Differential Drag-Based Orbital Maneuvers using Origami-Inspired Drag Area Modulation

Ayaz Ahmed

A thesis
submitted in partial fulfillment of the
requirements for the degree of

Master of Science in Aeronautics and Astronautics

University of Washington

2025

Committee:

Mehran Mesbahi

Avin Vijay

Program Authorized to Offer Degree:
Aeronautics and Astronautics

University of Washington

Abstract

Differential Drag-Based Orbital Maneuvers
using Origami-Inspired Drag Area Modulation

Ayaz Ahmed

Chair of the Supervisory Committee:
Mehran Mesbahi
Aeronautics and Astronautics

In recent years, a surge in demand for small satellites has generated interest in propulsionless orbital control methods—differential drag, specifically—as a way to minimize propellant usage and cost. While successful in a number of missions, present implementations typically limit this technique to an On-Off mode, which can limit maneuver flexibility and interfere with other mission requirements. This research introduces a continuous drag control system employing origami-inspired foldable structures. Such foldable panels allow for continuous modulation of the spacecraft's projected area, thus enhancing maneuver accuracy without sacrificing solar power or any other pointing related requirements.

Rendezvous maneuvers between two identical satellites are designed using linear equations, with battery State-of-Charge considerations. Results indicate that continuous control leads to a significant improvement over discrete On-Off control in terms of energy consumption for control inputs, while delivering equivalent performance. Additionally, incorporating additional degrees of freedom in origami design was proposed and evaluated, which significantly improved the power levels throughout the mission. A bar-and-hinge model is utilized to simulate dynamic unfolding behavior of the origami panels, and a proportional-integral-derivative control scheme is utilized for hinge actuation to achieve desired angles. Overall, this integrated approach not only optimizes differential drag control but is an efficient design for future small satellite missions with propellant-free orbital maneuvers.

TABLE OF CONTENTS

Page

List of Figures ii

Glossary iv

Chapter 1: Introduction 1
1.1 Differential drag as the actuator 2
1.2 Limitations of current methods and proposed solution 4
1.3 Origami in Space Application 6
1.4 Thesis Structure 6

Chapter 2: Theoretical Foundations 8
2.1 Origami Unfolding dynamics 8
2.2 Frames of reference for orbital dynamics 14
2.3 Equation of Motion 17
2.4 Aerodynamic Drag forces 20

Chapter 3: Problem Formulation and Methodology 22
3.1 Orbital maneuver 22
3.2 Optimizing Solar Efficiency with a Multi-Degree-of-Freedom Solar Panel . . 30

Chapter 4: Results and Discussion 36
4.1 Guidance and Optimal Control of Origami-based Spacecraft 36
4.2 Origami Control 47

Chapter 5: Conclusions 57
5.1 Future Efforts 59

Appendix A: Coordinate Frames transformation 65

Appendix B: Derivation of Hill's equation and Schweighart-Sedwick equations . . . 68

LIST OF FIGURES

Figure Number — Page

1.1 Historical account of Nanosat launches with prediction [1] . . . 2
1.2 Proposed mechanism for Origami based folding structures . . . 5

2.1 Schematic of Bar-and-Hinge Model . . . 8
2.2 N4B5 model of a Miura . . . 9
2.3 N5B8 model of a Miura . . . 10
2.4 Schematic of Bar element in equilibrium and disturbed state . . . 11
2.5 Schematic of force generated by folding spring [2] . . . 13
2.6 Frames used to describe the equations of motion, inspiration from work by Weiss et al.[3] . . . 15
2.7 Vector diagram for Chaser and Target Spacecraft . . . 18
2.8 Comparison of relative motion trajectories . . . 19
2.9 Schematic of projected area control . . . 21

3.1 Sketch illustrating linear relaxation . . . 26
3.2 Sketch illustrating approach to resolve $\|\hat{n}\| = 1$ constraint . . . 27
3.3 Proposed configuration of Solar panels . . . 31
3.4 Schematics of angles before and after γ actuation . . . 34
3.5 Relationship between θ_f and γ for varying θ_i's . . . 34

4.1 Phase Plot for uncontrolled case . . . 38
4.2 Phase plots for the two cases . . . 39
4.3 Evolution of control input(θ) over time . . . 39
4.4 Power generated with relaxed dynamics and actual dynamics . . . 40
4.5 Evolution of the norm of the unit vector $n(k)$ over time . . . 40
4.6 Phase plots for On-Off control and Continuous Control . . . 42
4.7 Comparison of control deployment for both the control schemes, for $d' = d$ . . . 43
4.8 Comparison of control deployment for both the control schemes, for $d' = d/3$ 43
4.9 Comparison of control deployment for both the control schemes, for $d' = d/5$ 44
4.10 Condition for maximum charging . . . 47
4.11 SoC data for different s_{min} cases . . . 48

4.12 SoC data for different s_{min} cases (figure continued) 49
4.13 Comparison of fixed panels and 3 degree of freedom panels 50
4.14 Schematic of the Origami model of the spacecraft with solar panels 51
4.15 Deployment of Solar Panels from stowed condition 52
4.16 PID $K_P = 10, K_I = 0.5, K_D = 0.5$ 54
4.17 PID $K_P = 15, K_I = 0.1, K_D = 0.01, \dot{\theta} = 1$deg/sec 54
4.18 PID $K_P = 15, K_I = 0.1, K_D = 0.01, \dot{\theta} = 0.1$deg/sec 55
4.19 Rate of change of θ for minimum time case 55
4.20 PID $K_P = 50, K_I = 5, K_D = 0.01, \dot{\theta} = 0.25$deg/sec 56

A.1 Vector diagram depicting the relation between different coordinate frames . . 66

GLOSSARY

DIFFERENTIAL DRAG: A maneuver technique utilizing differences in atmospheric drag forces acting on spacecraft to achieve relative orbital control without propulsion.

ORIGAMI-BASED STRUCTURES: Deployable structures inspired by the traditional Japanese art of paper folding, used in spacecraft to efficiently stow large surfaces into compact volumes.

FORMATION KEEPING: Maneuvering strategy to maintain the relative position and orientation of multiple spacecraft over extended durations.

MINIMUM-TIME RENDEZVOUS: A maneuver planning approach that aims to minimize the duration required to bring two spacecraft to the same location in orbit.

HILL'S FRAME: A rotating reference frame fixed to a target spacecraft in orbit, often used to describe relative orbital dynamics.

ECI FRAME: Earth-Centered Inertial Frame; a non-rotating coordinate system with its origin at Earth's center, commonly used to describe absolute positions and velocities of spacecraft.

LVLH FRAME: Local-Vertical Local-Horizontal Frame; an orbital coordinate system attached to the spacecraft, rotating with the spacecraft, commonly used for analyzing relative spacecraft dynamics during rendezvous and proximity operations.

CROSS-TRACK MOTION: Movement perpendicular to the orbital plane, which typically cannot be controlled using aerodynamic drag.

SCHWEIGHART-SEDWICK EQUATIONS: A set of linearized equations used to describe the relative motion of spacecraft during close-proximity maneuvers in orbit.

SEQUENTIAL CONVEX PROGRAMMING (SCP): An iterative optimization method that solves a sequence of convex approximations of a non-convex problem, converging towards a feasible solution.

BISECTION METHOD: A numerical method for solving optimization problems by iteratively narrowing down the feasible range of solutions by repeatedly halving the search interval.

STATE-OF-CHARGE (SOC): The percentage measure of the current charge capacity of a battery relative to its maximum possible charge.

RADIAL DIRECTION: The direction pointing outward from the Earth's center toward the spacecraft, typically denoted as the x-axis in relative orbital mechanics.

ALONG-TRACK DIRECTION: The direction aligned with a spacecraft's trajectory along its orbit.

NEUTRAL ANGLE: The hinge angle at which an origami structure experiences zero internal bending stress or torque in the absence of external forces.

BAR AND HINGE MODEL: A simplified structural representation used for modeling origami-based deployable structures, in which rigid panels are represented as bars connected by hinges, facilitating the analysis of structural deformation and dynamic behavior during folding or unfolding processes.

FOLDING HINGE: A structural hinge that allows segments of an origami-based structure to fold or unfold, actively controlled or passively set for deployment.

BENDING STIFFNESS: A property measuring a structural element's resistance to deformation when subjected to bending forces.

SOLAR IRRADIANCE: The power per unit area received from solar radiation, typically measured in watts per square meter (W/m^2).

PID CONTROLLER: A control strategy that combines proportional, integral, and derivative actions to minimize the error between a desired setpoint and the measured process variable.

INTEGRAL WINDUP: A phenomenon in PID controllers where the integral component accumulates error excessively, leading to prolonged deviation from desired system performance.

ACKNOWLEDGMENTS

Alhamdulillah, all praise be to Allah the Almighty of God the most Gracious and the most Merciful, first of all I would like to thank God for His blessings.

I extend my deepest gratitude to my advisor, Professor Mehran Mesbahi, whose unwavering guidance, encouragement, and belief in me have been invaluable. He has always given me the freedom to explore, challenge myself, and grow, providing support at every step of this journey.

I am also deeply thankful to Professor Avin Vijay for agreeing to be part of my thesis committee and taking time out of his busy schedule. His belief in my capabilities has been a great source of motivation.

I am also deeply thankful to my lab mates at RAIN Lab—my friends—for welcoming me, accepting me as part of the team, and giving me the opportunity to contribute to a group with a remarkable history and an even greater future. Being part of such a team has been an inspiring and enriching experience. To my friends outside the lab, who have always been there for me—offering support, joining me on hikes, dinners, and games, —thank you. Your companionship and encouragement have made this journey not only academically fulfilling but also personally rewarding.

I would also like to thank the Department of Aeronautics and Astronautics and the University of Washington for accepting me, providing an environment where I could learn and grow, and surrounding me with incredible people who have shaped my academic journey. The journey that would have been insurmountably tough without the love and encouragement from my family, whose support has been my unshakable source of strength.

The research presented in this thesis has been supported by National Science Foundation "CPS: Autonomy of Origami-inspired Transformable Systems in Space Operations" under Grant CPS-2201612.

DEDICATION

To my parents and my sisters, for their unwavering support, constant encouragement, and for always pushing me beyond my comfort zone.

Chapter 1

INTRODUCTION

Over the last decade, the space community has witnessed a sudden surge in the deployment of small satellites and this trend is predicted to continue in the coming years. This is evident from the recent statistics shown in Figure 1.1 taken form [1]. For example, a record-breaking 390 Nanosatellites (Nanosats) were launched in year 2023 alone. The total number of nanosats has crossed 2000 mark. It took 16 years to cross first 1000 mark and just 4 years to get to next 1000 mark [1]. This sudden surge is fueled by factors like innovation in the launch market allowing for cheaper launches, and availability of Commercial-of-the-Shelf (COTS) components facilitating faster and cheaper manufacturing. It is also pushed by organizations investing in satellite constellations, like Planet Lab Inc. [4] that deployed 72 CubeSats in 2023 [1].

However due to limited financial, mass and space budgets these small satellites are in need of an alternative to chemical propulsion systems, which are generally bulky and expensive. A viable and mission demonstrated alternative is to use differential drag, which leverages the difference in the relative drag between the two satellite to control the relative position of the satellites with respect to one another. This method is demonstrated in various previous missions. AeroCube-4 [5] (launched in 2012) was a scientific technology demonstrator, that consisted of three satellites with deployable "wings" to enhance drag and swap the relative positions of the three satellites. Planet Labs Inc. [4] is one of the most prominent users of this approach, operating an entire swarm of propulsion-less satellites that rely on differential drag for formation-keeping and conjunction avoidance [6, 7]. Similarly, the CYGNSS [8] mission relies on differential drag to adjust the spacing between its satellites and most of the conjunction avoidance maneuvers. NASA's EO-1 [9] satellite also demonstrated the said technique shortly after decommissioning, this also brought out the challenges of using differential drag on mission hardware which were not designed to be

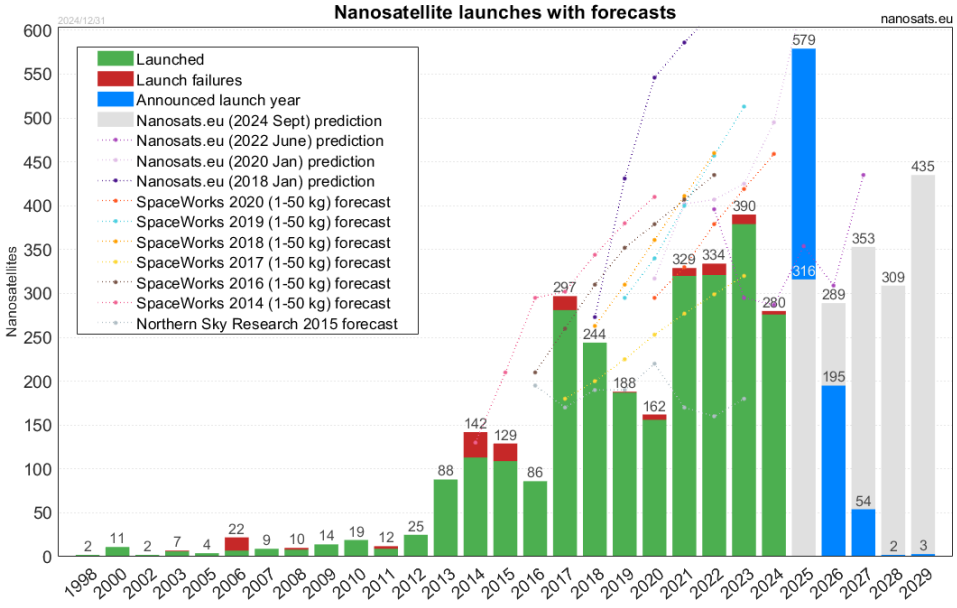

Figure 1.1: Historical account of Nanosat launches with prediction [1]

in high drag mode for longer durations.

In addition to fuel savings and avoiding chemical contamination from thrusters' plumes, the proposed method eliminates vibrations generated by thruster firings, which can disrupt sensitive onboard instruments. Differential drag methods can also serve as a reliable backup to traditional propulsion system in the event of loss of equipment or end of mission.

1.1 Differential drag as the actuator

Differential drag as an actuator for was first proposed by Leonard in her Master's thesis [10] and also in a follow-up work by Leonard et al. [11]. In her work, Leonard proposed adjusting the drag panels between high- and low-drag modes as a way to control the relative position between two satellites, she proposed a two-part control law, where the first (main) control works to minimize the position error and a second control that reduces eccentricity of the slave (chaser/secondary/follower) spacecraft. Subsequent works on the differential drag approach has mainly explored two distinct use cases: rendezvous maneuvers and formation

control, including formation-keeping and phasing.

Kumar and Ng [12] built upon Leonard's works [10, 11] by considering challenges associated with the practical implementation of the differential drag control in orbit. In their work, they considered multiple errors, perturbations and uncertainties that were mostly ignored in previous works. Bevilacqua and Romano [13] further enhanced previous works by considering the Schweighart-Sedwick [14] equations for system dynamics. They also proposed a closed-form, analytical formulation for rendezvous maneuver considering multiple spacecraft. In particular, they proposed a method where each chaser's secular motion is stabilized into a closed relative orbit around a target; and then, a relative eccentricity control zeroes the semi-axis for rendezvous. In a follow-on to this work, Bevilacqua [15] suggested a combination of drag based actuation as well as low thrust engines. The suggestion was to use differential drag to control chaser in the initial phase using analytically computed drag sequence then use low thrust propulsion system to optimally execute close proximity rendezvous operations. Harris and Açıkmeşe [16] presented a method to solve minimum time rendezvous problem involving multiple spacecraft. They used a relaxed convex optimization problem and showed the relaxed problem gives the solution for the original non-convex optimization problem. There are other works involving more advanced controls for the purpose. Perez and Bevilacqua [17] proposed a Lyapunov-based control strategy to manage the non-linear dynamics of the spacecraft while trying to follow an analytical guidance trajectory. Dell'Elce [18] et al. proposed a robust optimal control for the differential drag based maneuvers to account for uncertainties. Other works on rendezvous can be found in [19, 20, 21, 22, 23, 24, 25, 26, 27, 28, 29]

The second most studied scenario for differential drag applications is the formation-keeping of satellites. Practical mission implementation by CYGNSS [8] and Planet Labs Inc. [6] fall into this category. The foundation for this work was laid by Leonard [11] and a similar work was pursued by Mathews and Leszkiewicz [30]. In the meantime Fourcade, while carrying out mission analysis for the *Interferometric Wheel* proposed a differential drag based control for the mean nodal elongation between different satellites [31]. Foster et al. [7] proposed an elaborate differential drag based mission planning to achieve in-orbit phasing and then station-keeping for a constellation of several satellites. They also

proposed an optimization framework to assign the satellites in various slots depending on initial spread to achieve phasing in a time optimal manner. Other work on the topic can be found in [32, 33, 34, 35, 36, 37]

Although most of the work has explored rendezvous and formation-keeping scenarios, the conjunction avoidance has also been studied and extensively used in practical missions. Clark and Highsmith [38] recommended that spacecraft with perigee less than 560 km can avoid collisions by increasing the drag, by increasing the ballistic coefficient by a factor of 3 for 72 hours. However, they also noted that this constraint is highly impractical for a large number of satellites owing to other pointing requirements. Planet Labs' Dove spacecraft's example was presented where on average increase in ballistic coefficient was reported to be a factor of 3.2 [7], even though a maximum factor of 10 was possible.

1.2 Limitations of current methods and proposed solution

Orbital maneuver design using differential drag–although novel–has limitations such as the fact that the corresponding control can operate in only two modes. This lack of control authority limits certain aspects of control which will be examined further in the coming sections. Current methods rely on reorientation of the spacecraft by activating high drag mode. Current missions report that due to other mission related requirements such as imaging, communication, and battery charging, places constraints on the amount of time for which the spacecraft can be deployed in high drag mode, as reported by Foster[7] for Planet Lab satellite constellation. Additionaly, it was reported by Foster et al. [7], that while using differential drag for collision avoidance, the Planet Labs' Flock constellation can practically achieve ΔBC of close to 2, when in theory, it is possible to get a value of 9. This limitation is also attributed to other pointing requirements for communication and charging.

In summary, current differential drag techniques have two major practical limitations: first, the lack of continuous control, and second, constraints due to mission requirements. Very few attempts have been made to address the first issue and author is not aware of any attempt to resolve the second issue so far. Fanebust in his Master's thesis [39] proposed a method to control the Ballistic Coefficient (BC) by modulating the projected area to the

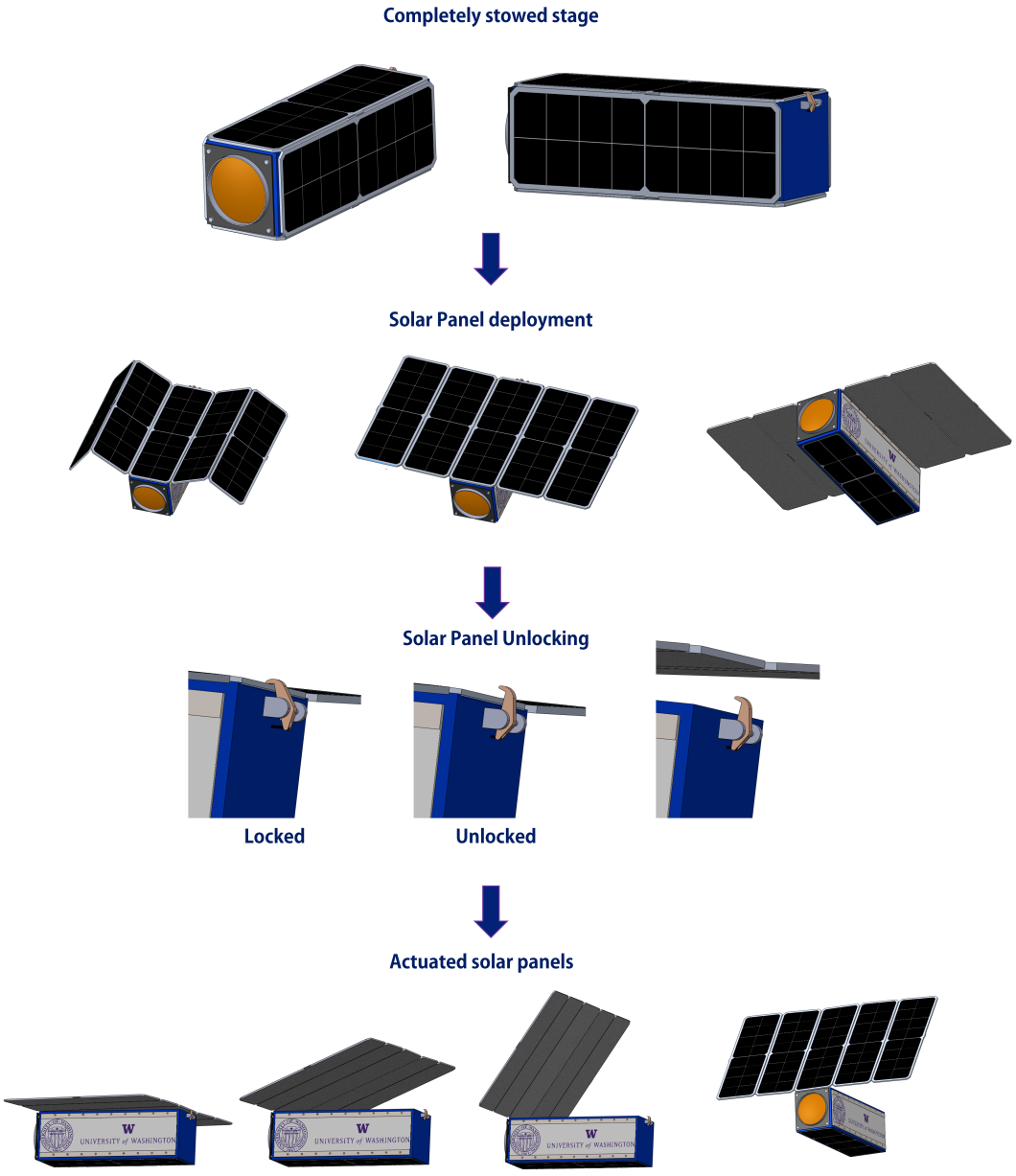

Figure 1.2: Proposed mechanism for Origami based folding structures

flow by controlling the attitude of the spacecraft. Although, this tackles the first problem, it exacerbates the second problem significantly. The first limitation is the lack of continuous control, and the second is constraints due to mission requirements.

This work proposes a foldable and controllable assembly to modulate the projected area of the spacecraft to tackle the aforementioned technical limitations simultaneously. By having a controllable folding mechanism, the area can be modulated in the continuous fashion, without changing the orientation of the spacecraft (see Figure 1.2). This solution is inspired by the Japanese art of paper folding, known as Origami.

1.3 Origami in Space Application

Origami is the ancient art of paper folding from Japan, which evolved from decorative and artistic pieces into a key piece of technology with applications in science and engineering. Traditionally, Origami has involved folding a flat sheet of paper into intricate structures without any cuts, allowing it to shrink a large surface area into a small volume, a property which makes it very lucrative to space system engineers for applications like solar arrays, antennas and sunshields, which can be stowed inside a low volume payload fairing of a rocket and can be deployed in the space. A prominent example is the James Webb Space Telescope(JWST) [40] that uses origami-like folding mechanism for its massive sunshield and primary mirror. Another application is stowed deployable solar panels for small satellites enabling efficient packaging. NASA's upcoming Starshade mission [41] deploys a massive shield to block the starlight to study the distant exoplanets. This massive structure is intricately folded into a small enough form factor to sit inside a rocket for launch.

1.4 Thesis Structure

This thesis is structured in multiple chapters, starting with Chapter 1 that introduces the topic and lays out the foundation for this work. This chapter discusses the prior work done in this field and brings out the shortcomings that the current work attempts to address.

In Chapter 2, the comprehensive theory involved in this work is brought out, starting with the modeling of the dynamic unfolding of an Origami structure. Then the concepts involving orbital dynamics are presented with the frame definitions. The equation of motion

are presented for relative state between two satellites. This is followed by a short discussion on atmospheric drag modeling.

In Chapter 3, problem statement is defined in mathematical terms, involving relative state dynamics and battery state-of-charge. The problem is then formalized as an optimization problem. The rest of this chapter examines control system design for the origami structure.

Finally in Chapters 4 and 5, the results of the work are presented, together with a detailed discussion of the observations made, followed by conclusions of the work and proposed future work.

Chapter 2

THEORETICAL FOUNDATIONS

In this chapter, we discuss the origami unfolding dynamics, followed by a brief presentation on reference frames and dynamics for proximity operations.

2.1 Origami Unfolding dynamics

Capturing the transient dynamics of an origami structure has been a fascinating field of work. Different models exist with varying levels of complexity and accuracy. This work uses a very popular method to carry out such simulation that is Bar-and-hinge model. The model is widely used due to its ease of use and intuitive nature, while also being flexible to account for complex transient mechanics. This model was first proposed by Schenk and Guest [42] and further enhanced by Filipov et al. [43].

This model falls under the class of Finite Particle Models(FPMs), since whole structure is represented as a collection of particles with finite mass connected through highly rigid structural ("bar") elements. The bar elements are like springs and simulate stretching of the structure. The bending and folding are simulated using torsional springs referred generally as "hinge" elements. These hinges lie between two facets, where a facet is a face formed by three or more connected particles. Folding and bending are both simulated using hinge elements. However, for bending, the hinge is much stiffer compared to the folding hinge. A

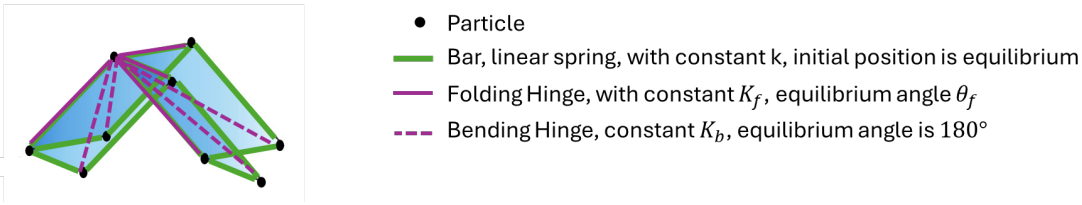

Figure 2.1: Schematic of Bar-and-Hinge Model

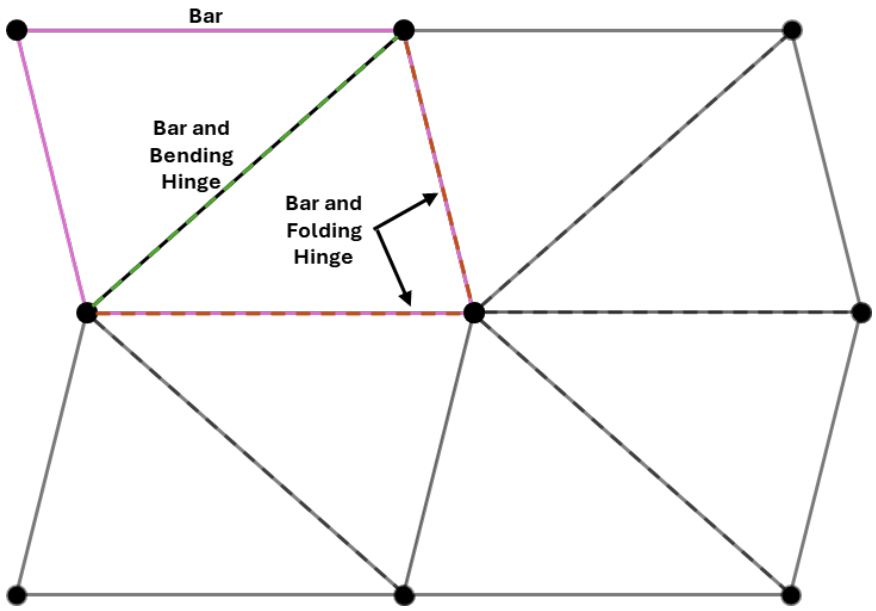

Figure 2.2: N4B5 model of a Miura

schematic of bars and hinges is shown in Figure 2.1 for a typical Miura element[44].

The main idea behind this model is to represent the complete origami structure as a network of finite mass particles connected through linear and torsional springs, then simulate the motion of each of the particle by superimposing the total force it experiences due to all the springs.

Discretization - First step to apply the bar-and-hinge model is to discretize the whole system into finite particles. For a single facet of a Miura element, there are two most common methods of discretization: one is N4B5 (Figure 2.2) and the other is N5B8 (Figure 2.3) configuration. Here the succeeding N represents the number of particles and the number succeeding B represents the number of Bars connecting those particles.

In N4B5 configuration, the single panel of the Miura pattern is represented by 4 particles placed at each vertex of the panel connected by 4 bar elements and a pair of diagonal particles are connected with a bar element which also acts as the torsional spring resisting the bending of the panel along this diagonal. However, in N5B8 configuration, there are 5 particles, 4 at vertex and one at the intersection of diagonals. Each vertex particle is connected with the

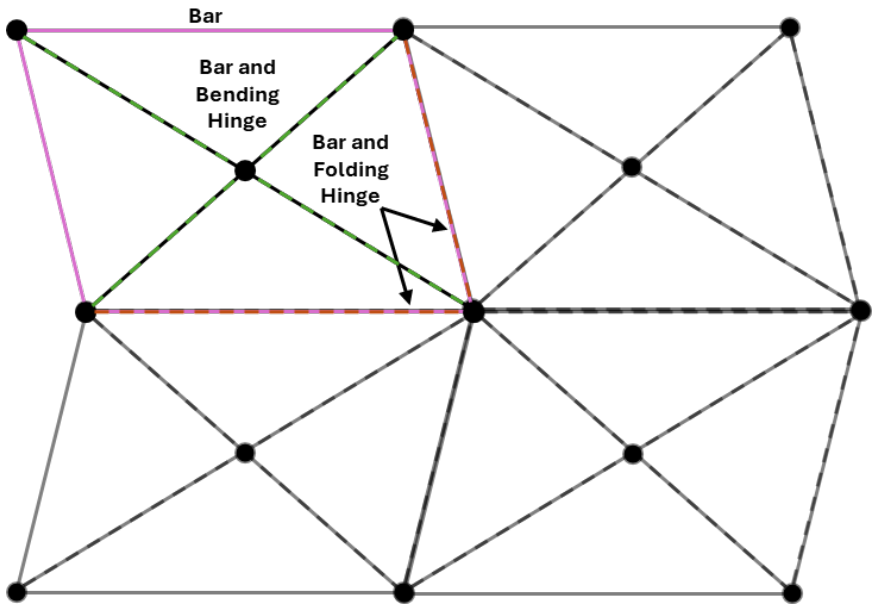

Figure 2.3: N5B8 model of a Miura

other through a bar element. Each of these particles is then also connected with the center particle through a bar element which is also a bending hinge for adjacent triangular panels. 4 such panels are connected in a single Miura Ori, the bar common to two panels also acts as the folding hinge as shown in Figures 2.2 and 2.3.

Filipov [43] and Liu and Paulino [45] presented a simple expression to calculate the thickness of each bar element and the mass of each particle. To do so consider a single triangular panel, in the N4B5 configuration, there are two such triangles and in the N5B8 configuration there are 4 such panels. The physical attributes of this panel govern the thickness of bars making this panel and the mass of particles at its edges. The cross sectional area of each bar in this panel is given as,

$$A_{bar} = \frac{2St}{(1-\nu)\sum_{i=1}^{3} L_i}. \tag{2.1}$$

where S is the area of the triangle, t is the thickness of panel, ν is the poisson's ratio of the material and $\sum_{i=1}^{3} L_i$ is the sum of length of all the bars making up this panel, which is also the perimeter of this panel.

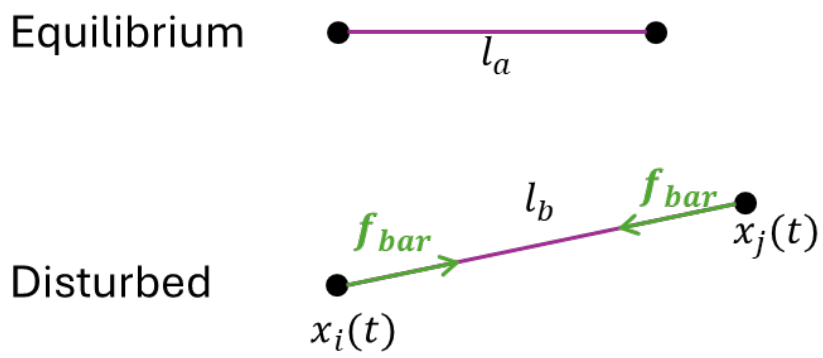

Figure 2.4: Schematic of Bar element in equilibrium and disturbed state

The mass of particles is calculated as the equal distribution of the total mass of the panel among the three particles on its vertices.

$$m_{\text{particle}} = \frac{1}{3} St\rho \tag{2.2}$$

where ρ is the density of the material. It is common for a particle or a bar to be part of multiple panels, in that case, the mass or the area should be superimposed from all the panels.

Particle Internal Force - First step in calculation of forces is finding the equilibrium positions of each particle and spring involved. Consider the case of no external load on the structure in this configuration, the dimensions of Miura are noted along with the angles of each folds. These folds become the equilibrium angle for these folds. **Bar force** - Consider a bar element as shown in Figure 2.4, connecting particles i and j with respective position of elements at time t being $x_i(t)$ and $x_j(t)$. The equilibrium length of this bar is noted as l_a while the current length is noted as $l_b = \|x_i(t) - x_j(t)\|$. Vector $\hat{\mathbf{x}}_{ij}(t) = (x_i(t) - x_j(t))/l_b(t)$ is the unit vector from particle j to i. The magnitude of bar force is given as

$$f_{bar}(t) = EA_{bar} \frac{l_b(t) - l_a}{l_a} \tag{2.3}$$

where E is the Young's Modulus. The force experienced by each particle and its direction

is expressed as

$$\mathbf{f}_{bar}^{i} = -f_{bar}\hat{\mathbf{x}}_{ij} \tag{2.4}$$

$$\mathbf{f}_{bar}^{j} = f_{bar}\hat{\mathbf{x}}_{ij} \tag{2.5}$$

Bending and Folding force - Bending and Folding forces are calculated in similar way as represented in this section. In figure 2.5, folding spring is considered, hence F superscript, however, force due to bending spring is calculated in similar fashion. In this configuration, there is a folding spring between particles k and j. The angle between the planes formed on either side of this spring is θ^F. The folding stiffness is expected to be a linear function of length of the spring. The folding stiffness(k^F) is written as,

$$k^F = K^F l^F \tag{2.6}$$

where K^F is the stiffness per unit length and l^F is the length of the spring in neutral condition. The restoring moment applied due to this spring is M^F, with neutral angle θ_0^F expressed as,

$$M^F = K^F l^F (\theta^F - \theta_0^F) \tag{2.7}$$

Now, this moment has to be expressed as the force experienced by each of the 4 particles involved.

The force experienced by particle i is straightforward and is expressed in terms of the perpendicular distance(d_i) from the crease jk.

$$\mathbf{f}_i^F = \frac{M^F}{d_i}\frac{\mathbf{m}}{\|\mathbf{m}\|} \tag{2.8}$$

$\mathbf{m}$ is the vector perpendicular to the plane formed by i, j and k with positive direction as shown in figure 2.5. Mathematically,

$$\mathbf{m} = (\mathbf{x}_i - \mathbf{x}_j) \times (\mathbf{x}_k - \mathbf{x}_j) \tag{2.9}$$

Similarly

$$\mathbf{n} = (\mathbf{x}_l - \mathbf{x}_j) \times (\mathbf{x}_k - \mathbf{x}_j) \tag{2.10}$$

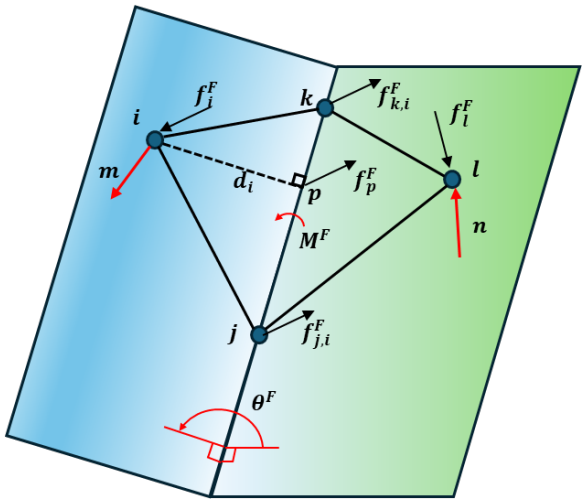

Figure 2.5: Schematic of force generated by folding spring [2]

To find the dihedral angle, the method proposed by Liu and Paulino[45] can be used as expressed below

$$\theta^F = \eta \cos^{-1}\left(\frac{\mathbf{m}\cdot\mathbf{n}}{\|\mathbf{m}\|\|\mathbf{n}\|}\right) \mod 2\pi,$$
$$\eta = \begin{cases} \operatorname{sgn}(\mathbf{m}\cdot\mathbf{r}_{kl}), & \text{if } \mathbf{m}\cdot\mathbf{r}_{kl} \neq 0, \\ 1, & \text{if } \mathbf{m}\cdot\mathbf{r}_{kl} = 0. \end{cases} \tag{2.11}$$

where $\mathbf{r}_{kl} = \mathbf{r}_k - \mathbf{r}_l$ An internal force of equal magnitude and opposite direction is applied at point p, then this force is distributed to the particle j and k, weighted by the inverse of the distance from the point p. Similarly, the force on particle l will be calculated and its contribution to the force on j and k is calculated. The net force on j (as well as k) is the sum of contribution from i and l .

$$\mathbf{f}_p^F = -\mathbf{f}_i^F$$

Then $\mathbf{f}_p^F$ is distributed among particle j and k

$$\mathbf{f}_{j,i}^F = \frac{l_{kp}}{l^F}\mathbf{f}_p^F$$
$$\mathbf{f}_{k,i}^F = \frac{l_{jp}}{l^F}\mathbf{f}_p^F$$

Final force are given as,

$$\begin{aligned} \mathbf{f}_j^F &= \mathbf{f}_{j,i}^F + \mathbf{f}_{j,l}^F \\ \mathbf{f}_k^F &= \mathbf{f}_{k,i}^F + \mathbf{f}_{k,l}^F \end{aligned} \tag{2.12}$$

This calculation is done for all the folding hinges as well as bending hinges. In case of bending hinges, the neutral angle is 180 which means all the surfaces are essentially flat in neutral case.

Once all the bar and hinge forces are calculated, and all the forces superimposed on particles, i.e., some particle will be experiencing multiple bar and hinge forces, so it is necessary to take the sum of all the forces. This force is denoted by $\mathbf{f}^{int}$, owing to internal nature of the force. A particle may also experience external force($\mathbf{f}^{ext}$), in the form of gravity, or external load. Particle will also experience damping to these movements, expressed as $\mathbf{f}^D = -\zeta m\dot{\mathbf{x}}$, with damping coefficient ζ. The position and velocity of individual particle is represented as $\mathbf{x}$ and $\dot{\mathbf{x}}$ respectively. So, now for each particle, equation of motion, can be written with initial conditions $\mathbf{x}_0$ and $\dot{\mathbf{x}}_0$

$$m\ddot{\mathbf{x}} = \mathbf{f}^{ext} + \mathbf{f}^{int} + \mathbf{f}^D \tag{2.13}$$

This equation has to be solved for each particle to get the new location of particles and recursively solve for new forces. Algorithm 1 illustrates the working of this method to solve for unfolding dynamics of the origami structure.

2.2 Frames of reference for orbital dynamics

2.2.1 ECI Frames

An Earth-Centered Inertial (ECI) frame is an important class of reference systems used in orbital dynamics, characterized by its origin at the Earth's center of mass and axes that do not rotate with the Earth. Instead, these axes maintain a fixed orientation relative to the distant stars, making ECI frames essential for describing the motion of satellites and spacecraft relative to Earth. Depending on the orientation of the axes, there can be different instances of ECI frame. The most commonly used frames are J2000 and GCRF frames.

J2000: A Standard ECI Frame J2000 is a specific instantiation of an ECI frame, defined by the positions of celestial bodies at the epoch of 12:00 TT on January 1, 2000. It

Algorithm 1 Particles Motion Simulation

Start
Set initial conditions, particle coordinates, element attributes, material properties.
loop
    Update the particle coordinates
    Calculate internal force due to bars' deformation. [Eq. (2.3)]
    Calculate internal force due to folding springs. [Eq. (2.8)]
    Calculate internal force due to bending springs. [Eq. (2.8)]
    Compute particle displacements at this step. [Eq. (2.13)]
    if this is the last time step **then**
        End
    else
        Proceed to the next step
    end if
end loop

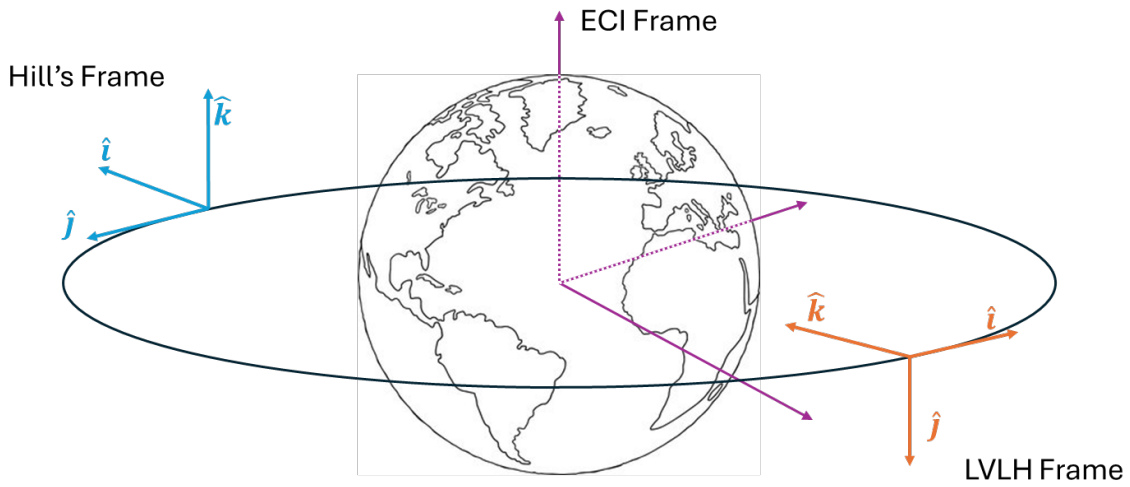

Figure 2.6: Frames used to describe the equations of motion, inspiration from work by Weiss et al.[3]

uses a precise orientation of axes based on the equinox and celestial poles at that time. An important distinguishing feature of J2000 is its Epoch-specificity i.e., the coordinates are based on the celestial configuration as of January 1, 2000.

Axis Orientation:

- **X-axis**: Points toward the mean vernal equinox at J2000.
- **Y-axis**: Completes the right-handed system, perpendicular to the X and Z axes, lying in the equatorial plane.
- **Z-axis**: Aligned with the Earth's rotational axis, pointing towards the North Celestial Pole.

GCRF: A High-Precision ECI Frame

The Geocentric Celestial Reference Frame (GCRF) is a more modern and precise ECI frame that aligns closely with the International Celestial Reference System (ICRS). GCRF defines an inertial frame using positions of distant quasars, providing the highest available measurement accuracy. This frame provides better precision and measurement accuracy by continuously updating to align with the ICRS. This frame dynamically adjusts for precession, nutation, and other minor celestial motions more accurately than J2000.

Axis Orientation:

- **X-axis**: Closely aligned with the J2000 mean equinox.
- **Y-axis**: Perpendicular to the X and Z axes, forming a right-handed coordinate system.
- **Z-axis**: Parallel to the mean spin axis of the Earth, pointing towards the North Celestial Pole.

2.2.2 LVLH frames

The LVLH frame, also known as the Local-Vertical/Local-Horizontal frame, is a rotating reference frame centered on an orbiting spacecraft. The LVLH frame simplifies the formulation of system dynamics, especially useful for maneuvering, docking, and attitude control.

The origin is fixed on the spacecraft(Target/Chief/Leader in most derivations). The Z-axis points towards the center of the Earth, and hence it is sometimes referred as Nadir-pointing LVLH frame. The Y-axis points away from the direction of angular momentum. And the X-axis completes the right-handed system. It should be noted that X-axis is not the direction of velocity only when the spacecraft is in circular orbit or is at the periapsis or apoapsis of the orbit. In all other cases, there is slight misalignment between the two depending on the eccentricity of the orbit.

Hill's frame, which will be employed throughout this work, closely resembles the LVLH frame but differs in axis orientation. In Hill's frame X-axis points away from the Earth in radial direction, Z-axis is in the direction of angular momentum and Y-axis completes the right-handed system. In doing so, Y-axis is almost aligned with the direction of the velocity of the spacecraft.

It should be noted that, these frames are fixed onto the spacecraft and are hence rotating as the spacecraft moves, which makes these frames non-inertial. But nevertheless expressing relative dynamics in the Hill's frame greatly reduce the complexity and gives more tractable equations of motions referred to as Hill's equations or in some literature a closed form solution is derived called Clohessy-Wiltshire equations. Both names are used interchangeably.

2.3 Equation of Motion

Hill's equations describe the relative motion of one spacecraft with respect to another spacecraft. Commonly used terms are Target and Chaser which will be used in this document. The reference frame used for this formulation is the Hill's frame which is fixed on the target spacecraft and follows the conventions of a typical Hill's frame. Hill's equations use the following two assumptions,

- The relative distance between the two spacecraft is much lesser compared to the radial distance from the center body(Earth).

- The target aircraft is in a circular orbit.

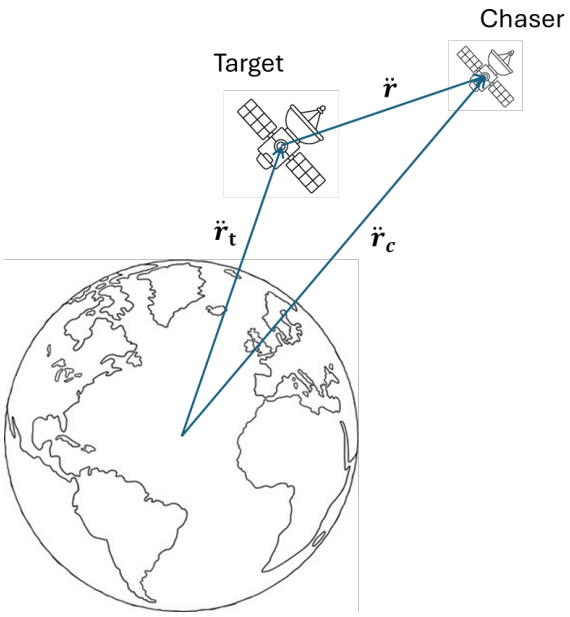

Figure 2.7: Vector diagram for Chaser and Target Spacecraft

Under these assumptions Hill's equation are written as,

$$\begin{aligned} \ddot{x} - 3n^2x - 2n\dot{y} &= 0 \\ \ddot{y} + 2n\dot{x} &= 0 \\ \ddot{z} + n^2z &= 0 \end{aligned} \tag{2.14}$$

Here, x, y, z are relative states of chaser spacecraft with respect to target spacecraft in Hill's frame. $x-$axis points in the radial direction away from the center, $y-$axis points in the direction of velocity and $z-$axis points in the direction of angular momentum. Directions y and z are also sometimes referred as along-track and cross-track directions respectively. The derivatives are also expressed in Hill's frame. Note that Hill's frame is non-inertial frame, so the velocity and acceleration transformations are not straightforward as position, when expressing in different frame of reference. Hill's equation (2.14), are linear, and captures the effects of gravitational attraction and orbital rotation without resorting to fully non-linear equations of motion. Under these equations, radial and along track motions get completely decoupled from the cross track motion. The cross track motion undergoes simple harmonic motion with frequency equal to the mean motion of the target spacecraft. The in-plane

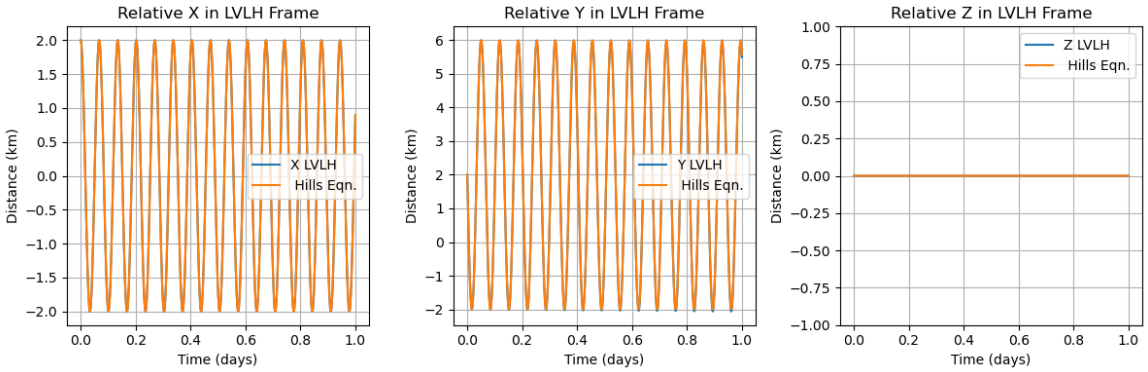

Figure 2.8: Comparison of relative motion trajectories

motion accounts for centrifugal and Coriolis forces due to rotating frame of reference.

In Figure 2.8, the equations' correctness was proved by performing a validation test on two satellites in formation. Two scenarios were simulated: Case 1, in which both satellites' orbital dynamics were propagated in Earth-Centered Inertial (ECI) and their resultant states were transformed to the Hill's frame for comparison; and Case 2, in which initial conditions were directly transformed to the Hill's frame and the Hill's equations were integrated. The relative motion computed by the two scenarios was found to have good agreement, verifying and confirming the derived equations' correctness. The good match is a strong confirmation of the formulation, and therefore, the equations accurately capture satellites' relative dynamics in formation flight.

While Hill's equations provide a simple linearized model for relative motion between satellites in near-circular orbits, they assume a perfectly spherical Earth and ignore the J_2 perturbation, leading to significant errors over extended durations or periods. The new formulation proposed by Schweighart and Sedwick, addresses this limitation by incorporating the effects of J_2 through a time-averaged gradient of the J_2 potential and by adjusting the reference orbit to include the secular and periodic effects of J_2. The resulting equations are linear and constant-coefficient, similar in form to Hill's equations, but they accurately

capture the relative motion of satellites under the influence of J_2. Specifically, the new equations modify the in-plane and cross-track frequencies and introduce a forcing term in the cross-track direction to account for differential nodal drift. Schweighart-Sedwick (SS) equations are expressed as,

$$\begin{aligned} \ddot{x} - (5c^2 - 2)n^2 x - 2nc\dot{y} &= 0 \\ \ddot{y} + 2nc\dot{x} &= 0 \\ \ddot{z} + q^2 z &= 2lq\cos(qt + \phi) \end{aligned} \tag{2.15}$$

These equations use an updated angular velocity of rotating frame to account for J_2 effects, by introducing the term c, where,

$$c = \sqrt{1 + s} \tag{2.16}$$

where

$$s = \frac{3J_2 R_e^2}{8r_{ref}^2}(1 + 3\cos(2i_{ref}))$$

where subscript ref corresponds to reference spacecraft i.e, target, J_2 is the J_2 coefficient associated to center body(Earth), R_e is the radius of Earth, r is the orbital radius and i is orbit inclination. The term s denotes the time-average of the J_2 gradient over one orbital period. Term q in (2.15) is the corrected cross-track frequency(refer AppendixB), while l and ϕ are calculated based on initial conditions. The forcing term in cross-track equation($2lq\cos(qt + phi)$) captures the differential nodal drift due to J_2 perturbations.

Under control forces for a chaser spacecraft with mass m, the equations can be written as,

$$\begin{aligned} \ddot{x} - (5c^2 - 2)n^2 x - 2nc\dot{y} &= \tfrac{1}{m}F_x \\ \ddot{y} + 2nc\dot{x} &= \tfrac{1}{m}F_y \\ \ddot{z} + q^2 z &= 2lq\cos(qt + \phi) + \tfrac{1}{m}F_z \end{aligned} \tag{2.17}$$

2.4 Aerodynamic Drag forces

The acceleration due to atmospheric drag on a spacecraft is similar to an aircaft, and is expressed as [10, 11]

$$\mathbf{a} = \left(-\frac{\rho A C_D}{2m} V^2 \right) \hat{V} \tag{2.18}$$

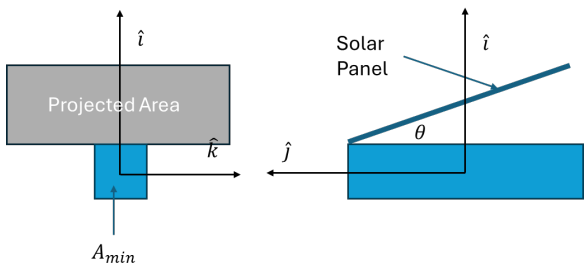

Figure 2.9: Schematic of projected area control

As seen in expression above(2.18), this is a function of atmospheric density(ρ), Coefficient of drag (C_D), mass of the spacecraft (m), velocity vector of the spacecraft ($\mathbf{V}$) and finally the reference area (A). In this work, the coefficient of drag is assumed to be independent of the projected area or the shape of the body. The atmospheric density is also assumed to be constant in this work. With these assumptions, at a given velocity, the acceleration experienced by a spacecraft depends linearly on the projected surface area. This work leverages this characteristic to modulate the projected surface area, thereby controlling the relative acceleration between the two spacecrafts and hence control the dynamics of relative position and velocity between the two spacecrafts.

As shown in the schematic in Figure 2.9, the total projected area is $A_{min} + A_0 \sin\theta$, where A_{min} is the cross section area in $\hat{i} - \hat{k}$ plane and is perpendicular to the velocity and A_0 is the total surface area of the solar panel.

In this work, the target spacecraft is assumed to be non-cooperating, hence cannot be controlled, which means the differential acceleration due to drag force will be computed assuming the projected area of the target spacecraft is A_{min} and that of the chaser spacecraft is $A_{min} + A_0 \sin\theta$. Here, angle θ can be controlled which will modulate the projected surface area and hence will control differential drag.

Chapter 3

PROBLEM FORMULATION AND METHODOLOGY

In this chapter we present the model and control design objectives for the developing differential drag-based orbital maneuvers.

3.1 Orbital maneuver

3.1.1 State dynamics

The problem considers relative states in in-plane, x (radial) direction and y (along-track) direction. Drag cannot exert forces out-of-plane; thus, the cross-track motion cannot be controlled. We assume, there is no cross track displacement, i.e., both satellites are in same plane. With these assumptions we are left with state $X = [x, \dot{x}, y, \dot{y}]^T$ and the linear equation is given as,

$$\frac{d}{dt}\begin{bmatrix} x \\ \dot{x} \\ y \\ \dot{y} \end{bmatrix} = \begin{bmatrix} 0 & 1 & 0 & 0 \\ b & 0 & 0 & a \\ 0 & 0 & 0 & 1 \\ 0 & -a & 0 & 0 \end{bmatrix} \begin{bmatrix} x \\ \dot{x} \\ y \\ \dot{y} \end{bmatrix} + \begin{bmatrix} 0 \\ \frac{F_x}{m} \\ 0 \\ \frac{F_y}{m} \end{bmatrix} \tag{3.1}$$

Here, $a = 2nc$ and $b = (5c^2 - 2)n^2$.

The study considers a propulsion-less spacecraft, which experiences no force other than drag, acting opposite to the velocity direction. A significant assumption in this study is that there exists a high bandwidth internal attitude controller on the chaser which asserts that body Y-axis is always aligned with that of the Hill's frame. This assumption significantly simplifies the problem. Under this assumption the specific differential force, $f_y = F_y/m$ can be calculated as, (assuming identical mass for target and chaser),

$$
\begin{aligned}
f_y = f_{Target} - f_{Chaser} &= \frac{1}{2}\rho v^2 A_{target} C_D/m - \frac{1}{2}\rho v^2 A_{chaser} C_D/m \\
&= \frac{1}{2m}\rho v^2 C_D (A_{target} - A_{chaser}) \\
&= \frac{1}{2m}\rho v^2 C_D (-A_0 \sin\theta) \\
&= -\frac{1}{2}\rho v^2 \Big(\frac{C_D A_o}{m}\Big) \sin\theta \\
f_y &= -\frac{1}{2}\frac{\rho v^2}{BC_0} \sin\theta
\end{aligned}
$$

where, ρ is the air density at the altitude, v is the orbital velocity, θ is the angle panels make with the body. The value of angle θ goes from $0°$(Minimum drag phase) to $90°$(Maximum drag phase). There is no force in x direction.

Now in current configuration, only chaser can be controlled, while target is non-cooperative. The unit vector normal to the solar panel for the chaser is considered as the control input for this dynamics, $n_c = [\cos\theta, \sin\theta]^T$. Finally, dynamics can be written in familiar non-linear form, $\dot{X}(t) = AX(t) - B\hat{n}_c(t)$,

$$
X = \begin{bmatrix} x \\ \dot{x} \\ y \\ \dot{y} \end{bmatrix}, \qquad A = \begin{bmatrix} 0 & 1 & 0 & 0 \\ b & 0 & 0 & a \\ 0 & 0 & 0 & 1 \\ 0 & -a & 0 & 0 \end{bmatrix}, \qquad B = \begin{bmatrix} 0 & 0 \\ 0 & 0 \\ 0 & 0 \\ 0 & d \end{bmatrix} \tag{3.2}
$$

where, $d = \frac{1}{2}\frac{\rho v^2}{BC_0}$ For typical values of a and b, matrix A has unstable eigenvalues but the system(A, B) is controllable. However in this case, the control input n_c is limited to only positive values, because of which not all the initial states can be driven to zero, which essentially means, rendezvous is not possible for all the initial states. This restriction actually comes from the fact that only chaser is controllable, while target is non-cooperative. This can be concluded intuitively too, consider two masses moving in straight line with some velocity and aerodynamic drag force, the relative distance can be made zero only when the controllable body is ahead of the non-controllable body, since both have same minimum drag.

For the configuration, where target too is controllable, the dynamics can be re-written

as,

$$\dot{X}(t) = AX(t) - B\hat{n}_c(t) + B\hat{n}_t(t) \tag{3.3}$$

for identical spacecrafts, where subscripts c and t refers to chaser and target spacecraft respectively.

3.1.2 Battery State-of-Charge(SoC) dynamics

This part of problem uses a simple first principle understanding of a battery discharge procedure, which says the rate of change of charge or energy content of the battery is equal to the difference in rate of energy gained(charging) and rate of energy lost(discharging).

Charging - Charging rate is directly related to the efficiency of solar panels, area of the solar panels, solar irradiance, and the angle between the panels and the sun direction.

$$P_{in} = \eta_{panel} A_{panel} I_{sun}(t) \max(0, \nu(t)) \tag{3.4}$$

where $\nu(t)$ represents the angle between the solar panels and the incoming solar rays. $n(t)$ is the unit vector perpendicular to solar panel and $v(t)$ is unit vector in the direction of sun from the body. So, $\nu(t) = \hat{n}(t)^T \hat{v}(t)$.

Discharging - Discharging can be represented as the average power load consumed by the spacecraft.

With this the SoC(denoted as s) dynamics can be written as,

$$\dot{s} = \frac{1}{E_{max}} \Big(\eta_{batt} (\eta_{panel} A_{panel} I_{sun}(t) \max(0, \nu(t)) - P_{load}(t) \Big)$$

where, E_{max} is the maximum capacity of the battery. Due to the short duration of the maneuver, solar irradiance can be considered constant. The power load can also be assumed constant taking average value. With this assumption, we get

$$\dot{s} = \alpha \max(0, \nu(t)) - \beta \tag{3.5}$$

3.1.3 Minimum time optimization problem

The primary requirement is to complete the maneuver in the shortest possible time, which has implications on overall mission duration. It is also important to note that when spacecraft spends longer time in high drag mode, it is losing energy at a faster rate. The battery

charge must be maintained above a certain level at all times. So the continuous time optimal control problem can be formulated as,

$$\min_{\hat{n}(t)} \int_0^{t_{\text{final}}} 1 \, dt$$

subject to

$$\begin{aligned} \dot{X}(t) &= AX(t) - B\hat{n}_c(t), \\ \dot{s}(t) &= \alpha \max(0, \nu(t)) - \beta, \\ s(t) &\geq s_{\min}, \\ \|\hat{n}_c(t)\| &= 1. \\ X(t_{\text{final}}) &= \mathbf{0} \end{aligned}$$

The equations are better expressed in discrete form,

$$X[k+1] = A_d X[k] - B_d \hat{n}_c[k], \quad k = 0, 1, ..., N-1 \tag{3.6}$$

$$s[k+1] = s[k] + \alpha_d \max(0, \nu(k)) - \beta_d, \quad k = 0, 1, ..., N-1 \tag{3.7}$$

$$s[k] \geq s_{min}, \quad k = 0, 1, ..., N \tag{3.8}$$

$$\|\hat{n}_c[k]\| = 1, \quad k = 0, 1, ..., N \tag{3.9}$$

$$X[N] = \mathbf{0} \tag{3.10}$$

In this formulation, only chaser is controlled, so control input $\hat{n}_c(t)$ corresponds to chaser's unit vector. Consider discrete system dynamics, (3.6), it is a linear system and hence does not need any extra work. $A_d = Adt + I$ and $B_d = Bdt$ where dt is time interval for discretization.

Battery dynamics (3.7) is convex but non-linear. We introduce a slack term $w(k)$, such that

$$w[k] \geq 0, \quad w[k] \geq \nu[k] = \hat{n}_c[k]^T \hat{v}[k] \tag{3.11}$$

this gives a linear constraint for battery dynamics,

$$s[k+1] = s[k] + \alpha_d w[k] - \beta_d, \quad k = 0, 1, ..., N-1 \tag{3.12}$$

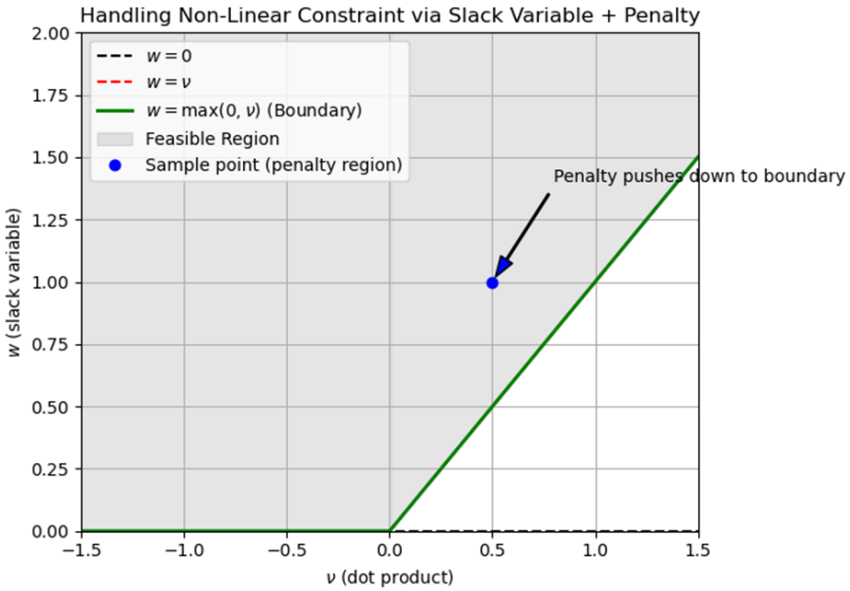

Figure 3.1: Sketch illustrating linear relaxation

where $\alpha_d = \alpha dt$ and $\beta_d = \beta dt$. To ensure that this relaxed dynamics closely approximates the actual non-linear behavior, a penalty term is introduced for $w[k]$. The term $\lambda \sum_{k=0}^{N} w[k]$ is added to the objective function to be minimized, this forces $w[k]$ to be minimal while maintaining the constraints, essentially pushing it to the actual non-linear function. λ is a penalty scaling term. The sketch for this relaxation in shown in figure 3.1

Equation (3.9) is challenging to handle within standard convex optimization tools because $\|\hat{n}[k]\| = 1$ is both non-convex and nonlinear. Here, general $\hat{n}$ is considered, the approach will be identical for chaser as well as target. To address this, we apply Sequential Convex Programming (SCP). The primary idea of SCP is to iteratively approximate the non-convex constraint with a convex surrogate function around a current reference point and then solve a convex subproblem in each iteration. Consider the function $F[k]$,

$$F[k] = \|\hat{n}[k]\| - 1 \tag{3.13}$$

which is non-convex. We linearize $F[k]$ around a reference point $n_{ref}[k]$, which yields,

$$f_k = \|\hat{n}_{ref}[k]\| - 1 + \frac{\hat{n}_{ref}[k]}{\|\hat{n}_{ref}[k]\|}(\hat{n}[k] - \hat{n}_{ref}[k]) \tag{3.14}$$

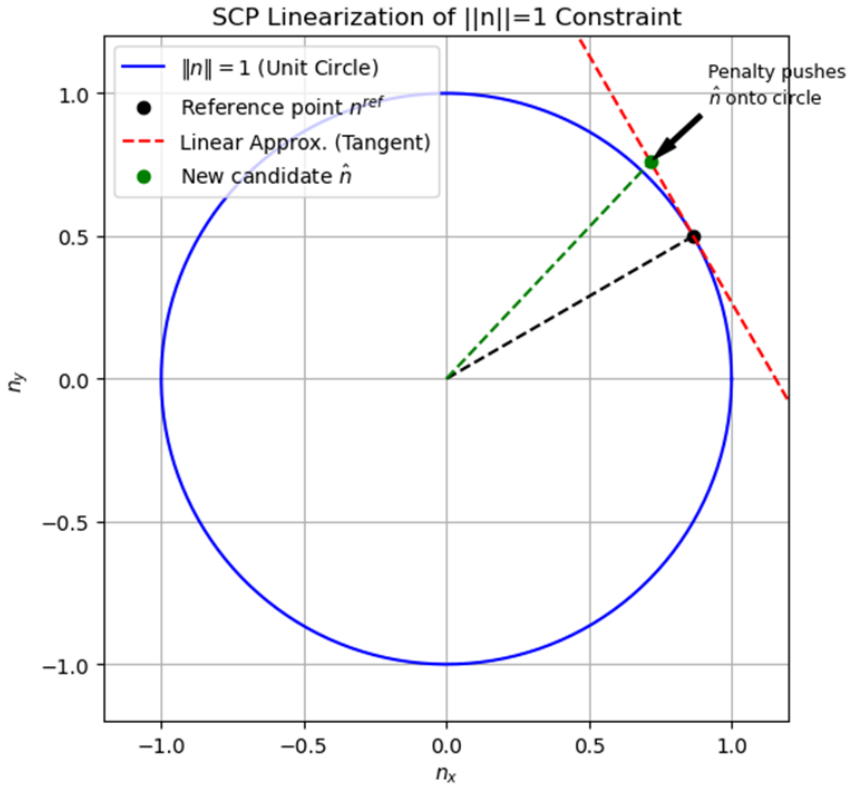

Figure 3.2: Sketch illustrating approach to resolve $\|\hat{n}\| = 1$ constraint

Equation (3.14) is a linear function in $\hat{n}[k]$, which makes it easier to add as a penalty term in optimization problem as $\mu \sum_{k=0}^{N} |[f[k]|$, where μ is a large penalty term. Figure 3.2 illustrates this approach.

In problems where time is divided into discrete steps $k = 0, 1, \ldots, N$ the minimum-time objective can be reinterpreted as finding the smallest integer N such that a set of constraints is satisfied. Concretely:

For a fixed integer N, consider whether there exists a sequence of decision variables that satisfies all system constraints like system dynamics. If a solution is found for a particular N, the problem is feasible for that N. Otherwise, it is infeasible.

Among all feasible values of N, the goal is to identify the smallest feasible N^*. This N^* corresponds to the fewest discrete steps (or the shortest total time $T = N^* \Delta t$ if each step

is of fixed duration Δt) needed to meet the constraints.

This transforms "minimize T" into an integer feasibility search:

"Find the smallest integer N for which the constraints are satisfied".

A basic approach would be to check feasibility in ascending order of N, from $N = 1$ upward, stopping at the first feasible point. This strategy, however, becomes computationally expensive if N^* is large or if the feasibility checks themselves are demanding. The run time can grow linearly with the size of the interval $[1, N^*]$.

Employing a bisection method—also known as binary search on N—significantly reduces computational effort by employing a logarithmic search pattern rather than a linear one. The bisection routine calls the feasibility solver only $\mathcal{O}(\log(\Delta N))$ times, where ΔN is the initial span $(N_{\text{high}} - N_{\text{low}})$.

Algorithm 2 Bisection Method for Minimum-Time Problem

Input: Infeasible lower bound N_{low}, Feasible upper bound N_{high}
while $(N_{\text{high}} - N_{\text{low}} > 1)$ **do**
    $N_{\text{mid}} \leftarrow \left\lfloor \frac{N_{\text{low}} + N_{\text{high}}}{2} \right\rfloor$
    feasible $\leftarrow$ CheckFeasibility(N_{mid})
    if *feasible* **then**
        $N_{\text{high}} \leftarrow N_{\text{mid}}$
    else
        $N_{\text{low}} \leftarrow N_{\text{mid}} + 1$
    end if
end while
Output: The smallest feasible N (either N_{low} or N_{high} after the loop)

After the bisection algorithm identifies the candidate value of N for which feasibility must be verified, a convex optimization check is carried out for each iteration until convergence. The feasibility subproblem is given in (3.15). The constraints include the system dynamics, and linearized battery SoC dynamics. An additional constraint ensures the battery's SoC

never falls below s_{min}. Instead of hard constraint on final $X[N]$, a soft constraint is imposed to ease computation in form of $\|X[N]\|_2 \leq \epsilon$.

After formulating the constraints and objective function, the convex optimization solver is executed. If the solver returns a feasible solution, the reference n_{ref} is updated to the new $n[k]$, and the iteration proceeds. Convergence is typically monitored by changes in the objective or differences in successive solutions, stopping once these measures remain below a specified tolerance. If the solver fails to find a feasible point or concludes that the problem is infeasible, the overall bisection process recognizes the infeasibility of this particular choice of N.

This iterative procedure is repeated at each bisection step. By combining a robust convex solver for each feasibility check with the linearized approximation of the non-convex norm constraint, the algorithm can efficiently explore different horizons N in search of the smallest feasible value that meets all problem requirements.

$$\text{minimize} \quad \lambda \sum_{k=0}^{N-1} w[k] \; + \; \mu \sum_{k=0}^{N-1} |f[k]|$$

subject to:

$$\begin{aligned}
&X[k+1] = A_d\, X[k] - B_d\, \hat{n}_c[k], \quad k = 0, \ldots, N-1, \\
&s[k+1] = s[k] + \alpha_d\, w[k] - \beta_d, \\
&w[k] \geq \hat{n}_c[k]^T \hat{v}[k], \\
&0 \leq w[k] \leq 1, \\
&\|\hat{n}_c[k]\|_2 \leq 1, \\
&s[k] \geq s_{\min}, \\
&X[0] = X_0, \quad s[0] = s_0, \\
&\|X[N]\|_2 \leq \epsilon.
\end{aligned} \tag{3.15}$$

This problem can be augmented to account for the case where both satellites can be controlled, simply by including the control terms associated with the target in the dynamics, and subsequently the constraints on target control are added to the formulation, as shown in (3.16). Note that in equation, (3.16), subscript t is used for target spacecraft, while

subscript c is used for chaser. This problem statement is just the extension of (3.15) with added term in dynamics and all the constraints on target spacecraft control too.

$$\text{minimize} \quad \lambda \sum_{k=0}^{N-1} w[k] \; + \; \mu \sum_{k=0}^{N-1} |f[k]|$$

subject to:

$$X[k+1] = A_d\, X[k] - B_d\, \hat{n}_c[k] + B_d\, \hat{n}_t[k], \quad k = 0, \ldots, N-1,$$

$$\begin{aligned}
&s_c[k+1] = s_c[k] + \alpha_d\, w_c[k] - \beta_d, \\
&w_c[k] \geq \hat{n}_c[k]^T \hat{v}[k], \\
&0 \leq w_c[k] \leq 1, \\
&s_c[k] \geq s_{\min}, \\
&\|\hat{n}_c[k]\|_2 \leq 1,
\end{aligned} \tag{3.16}$$

$$\begin{aligned}
&s_t[k+1] = s_t[k] + \alpha_d\, w_t[k] - \beta_d, \\
&w_t[k] \geq \hat{n}_t[k]^T \hat{v}[k], \\
&0 \leq w_t[k] \leq 1, \\
&s_t[k] \geq s_{\min}, \\
&\|\hat{n}_t[k]\|_2 \leq 1,
\end{aligned}$$

$$\begin{aligned}
&X[0] = X_0, \quad s_c[0] = s_{c_0}, \quad s_t[0] = s_{t_0}, \\
&\|X[N]\|_2 \leq \epsilon.
\end{aligned}$$

3.2 Optimizing Solar Efficiency with a Multi-Degree-of-Freedom Solar Panel

In next section, the results from the analysis will be discussed. In Figure 4.10a of results and the discussion around it, it is shown that for a fixed solar panel, the maximum amount of solar exposure possible is greatly limited, because of single degree of freedom. However,

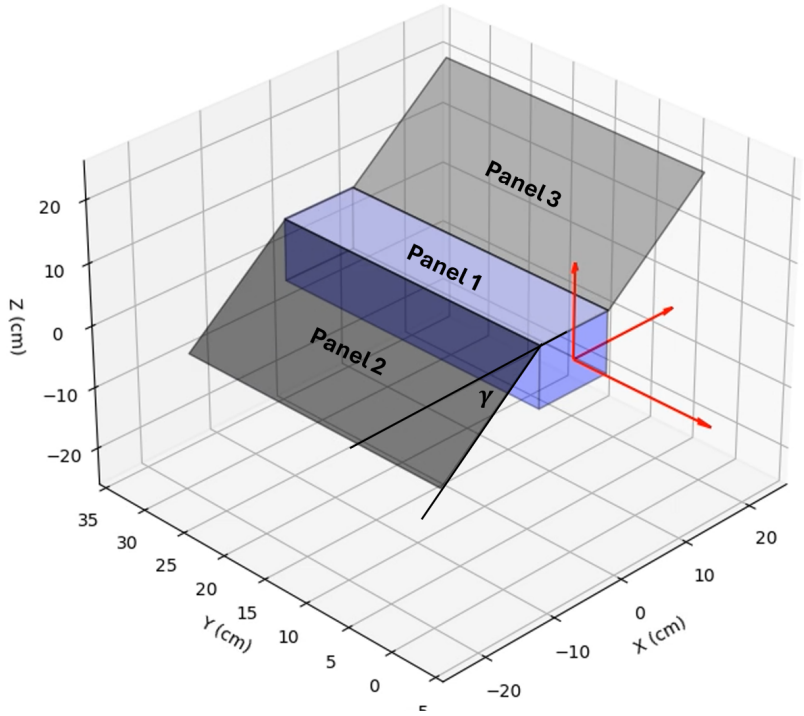

Figure 3.3: Proposed configuration of Solar panels

true advantage of origami-based structure is incorporating multiple degrees of freedom to fully utilize the concept. Based on this background, a new configuration is proposed as shown in Figure 3.3. In this configuration, the solar panel is split into three panels, panel 1 is the panel attached to the main satellite body, at the shorter edge, this fold is actuated as per the previous analyses for projected area modulation. Panel 2 and 3 are attached to panel 1 along length on either edges and the angle γ is controlled. To maximize solar exposure, Panels 2 and 3 are kept parallel, since, angle to maximize solar exposure is same for both the panels. Two assumptions are made here: first, the Coefficient of drag of the configuration does not change with the orientation of the panels, and second, the cross-track force on the body is negligible due to the panels. With these assumptions, the total drag on the body can be represented as only the function of projected area on $X - Z$ plane.

The proposed mechanism operates as follows, at any given time, the projected area for a trajectory is calculated assuming all the panels are moving together, i.e., single degree of

freedom. There is an associated angle $\theta(k)$ between the solar panel and the body of the satellite. In this configuration, panel 2 and panel 3 are rotated by angle γ ($-\gamma$ for Panel 3) such that the solar exposure is maximized while simultaneous changing(increasing) angle θ to keep the projected area same as calculated previously. Since the projected area does not change, the drag is same and hence the dynamics and trajectory is unaffected, however the solar exposure and hence battery charging is maximized.

The initial angle between the solar panel 1 and satellite body is θ_i. When panels 2 and 3 are rotated by angle γ, to maintain same projected area, angle θ increases to θ_f. The schematic explaining these angles are shown in figure 3.4. The expression relating these angles to each other are derived below.

For given angles θ and γ, the unit normal vector for panels 1,2, and 3 are expressed as,

$$\hat{\mathbf{n}}_\mathbf{1} = [\cos\theta, \sin\theta, 0] \tag{3.17}$$

Before γ rotation, normal unit vector of panel 1, 2, and 3 are identical $\hat{\mathbf{n}}'_\mathbf{2} = \hat{\mathbf{n}}_\mathbf{1}$. At this point the panel 2 is rotated by angle γ about the longer edge, $\mathbf{v_1}$, which is obtained by rotating vector $\mathbf{v_0} = [0, 1, 0]$ about Z-axis by θ.

$$\mathbf{v_1} = R_z(\theta)\mathbf{v_0} = \begin{bmatrix} \cos\theta & -\sin\theta & 0 \\ \sin\theta & \cos\theta & 0 \\ 0 & 0 & 1 \end{bmatrix} \begin{bmatrix} 0 \\ 1 \\ 0 \end{bmatrix} = [-\sin\theta, \cos\theta, 0] \tag{3.18}$$

Next, $\hat{\mathbf{n}}_\mathbf{2}$ is obtained by rotating $\hat{\mathbf{n}}'_\mathbf{2}$ about vector $\mathbf{v_1}$ by γ. Using Rodrigues' rotation formula,

$$\hat{\mathbf{n}}_\mathbf{2} = \hat{\mathbf{n}}'_\mathbf{2}\cos\gamma + (\mathbf{v_1} \times \hat{\mathbf{n}}'_\mathbf{2})\sin\gamma + \mathbf{v_1}(\mathbf{v_1} \cdot \hat{\mathbf{n}}'_\mathbf{2})(1 - \cos\gamma) \tag{3.19}$$

Now,

$$\mathbf{v_1} \times \hat{\mathbf{n}}'_\mathbf{2} = \begin{vmatrix} \hat{\mathbf{i}} & \hat{\mathbf{j}} & \hat{\mathbf{k}} \\ -\sin\theta & \cos\theta & 0 \\ \cos\theta & \sin\theta & 0 \end{vmatrix} = [0, 0, -1]$$

$$\mathbf{v_1} \cdot \hat{\mathbf{n}}'_\mathbf{2} = (-\sin\theta)(\cos\theta) + (\cos\theta)(\sin\theta) = 0$$

Putting it back in (3.19),

$$\hat{\mathbf{n}}_\mathbf{2} = \hat{\mathbf{n}}_\mathbf{3} = [\cos\theta\cos\gamma, \sin\theta\cos\gamma, -\sin\gamma] \tag{3.20}$$

Projected area in single degree of freedom case is given as,

$$A_{proj} = A_{panel}\sin\theta \tag{3.21}$$

For multiple degree of freedom case, individual projected areas are added. The area of Panel 1 is taken as $0.2A_{panel}$ while the area of panel 2 and 3 is identical and is equal to $0.4A_{panel}$. So the projected area after rotation is given below

$$A'_{proj} = 0.2A_{panel}\sin\theta + 0.8A_{panel}\sin\theta\cos\gamma \tag{3.22}$$

To maintain same projected area through rotation γ, angle θ_i changes to θ_f, so combining equation (3.21) and (3.22) will give,

$$\sin\theta_i = \sin\theta_f(0.2 + 0.8\cos\gamma) \tag{3.23}$$

The result from this expression is plotted in Figure 3.5. In this Figure, the variation of θ_f with γ is plotted for different θ_i's. As seen in the Figure, for a given θ_i, θ_f increases with γ which is expected. It should also be noted that since maximum θ_f is fixed at 90°, the range of allowable γ is also limited. This range is small for higher values of θ_i, it is zero for $\theta_i = 90°$ and unbounded for $\theta_i = 0°$ because in this case changing γ does not affect the projected area.

The battery dynamics equation (3.7) in this case(3 degree of freedom) is written as,

$$s[k+1] = s[k] + \alpha_d w_{3\text{DOF}}[k] - \beta_d \tag{3.24}$$

where,

$$w_{3\text{DOF}}[k] = 0.2\max(0, \hat{\mathbf{n}}_\mathbf{1}(\theta_f)\cdot v[k]) + 0.8\max(0, \hat{\mathbf{n}}_\mathbf{2}(\theta_f)\cdot v[k]) \tag{3.25}$$

The procedure to obtain maximum value of $w_{3\text{DOF}}$ and corresponding γ for given trajectory, is explained in Algorithm 3. For a given θ_i an exhaustive search is carried out between the bounds of γ to calculate maximum value of $w_{3\text{DOF}}$ and the corresponding γ_{best}. For every possible value of γ, $\sin\theta_f$ is calculated and ensured its value is in $[0, 1]$, subsequently for this feasible γ ,$w_{3\text{DOF}}$ is calculated and compared against previous values.

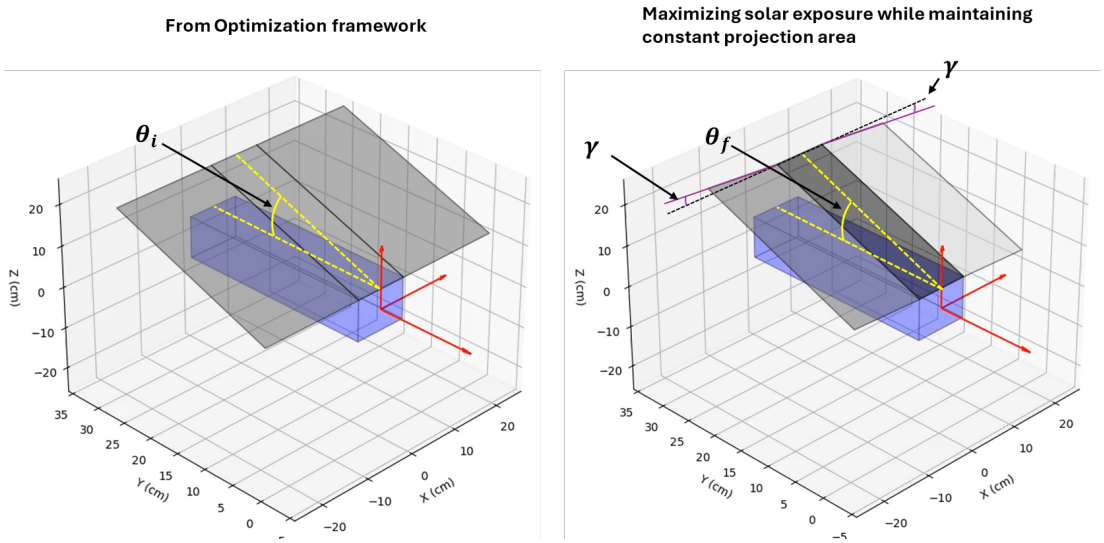

Figure 3.4: Schematics of angles before and after γ actuation

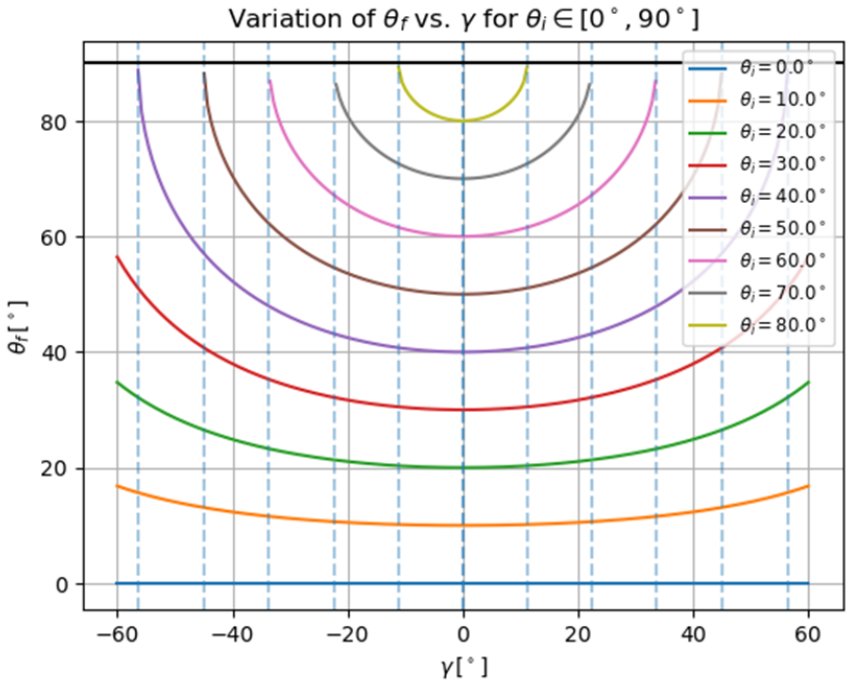

Figure 3.5: Relationship between θ_f and γ for varying θ_i's

Algorithm 3 Algorithm for Optimal Trajectory with γ-Maximized w_{3DOF}

Require: Initial parameters, γ_0

Ensure: Optimal trajectory with associated γ values maximizing w_{3DOF}

Step 1: Trajectory Optimization
Run trajectory optimization algorithm to obtain optimal trajectory parameters $\{\theta_i\}_{i=1}^{N}$
Step 2: Maximize w_{3DOF} for Each θ_i
for each θ_i in $\{\theta_1, \ldots, \theta_N\}$ **do**
    Initialize $\gamma_{\text{best}} \leftarrow 0$, $w_{\text{3DOF}}^{\max} \leftarrow -\infty$
    for $\gamma \in [-\gamma_0, +\gamma_0]$ (exhaustive search) **do**
        Compute $\sin(\theta_f)$ using Equation (3.23)
        if $0 \leq \sin(\theta_f) \leq 1$ (validity check) **then**
            Calculate w_{3DOF} associated with γ using Equation (3.25)
            if $w_{\text{3DOF}} > w_{\text{3DOF}}^{\max}$ **then**
                Update $w_{\text{3DOF}}^{\max} \leftarrow w_{\text{3DOF}}$
                Update $\gamma_{\text{best}} \leftarrow \gamma$
            end if
        end if
    end for
    Store γ_{best} for θ_i
end for
Step 3: Return
Return optimized trajectory with $\{\gamma_{\text{best}}\}$ values

Chapter 4

RESULTS AND DISCUSSION

In this chapter we discuss the results obtained by models and the control design methodology presented in previous chapters involving differential drag maneuvers via origami panels.

4.1 Guidance and Optimal Control of Origami-based Spacecraft

The parameters used in the study are listed in table 4.1. The parameters are adopted from Harris and Açıkmeşe [16], who solved for time-optimal trajectories using an on-off controller without constraints related to pointing requirements. Parameters associated with battery SoC dynamics are mentioned in table 4.2 The initial condition considered is $x_0 = [-0.53, 0.25, -0.48, 3.31]$ where length unit is in km and time is in $hour$. However for the case where only the chaser is controllable, this initial point is not stabilizable and hence $-x_0$ is considered for that case. For the first few cases the required minimum battery state of charge is kept low($s_{min} = 0\%$), to observe the advantage associated with just having continuous control over ON-OFF control. The ratio between penalty scaling terms μ and λ is maintained at 10. The orbital parameters for target corresponding to the values of a and b can be calculated as follows, orbital radius $r_{target} = 6724.87km$, eccentricity of zero, inclination $i = 81.53°$. For the case where satellite is never in the shadow, following parameters were chosen, start time for maneuver is '2023-06-21 12:00:00', with RAAN of 185° and true anomaly of 90°

Before presenting the controlled cases, an uncontrolled case is shown in Figure 4.1, As evident from the figure, the system is unstable with eigenvalues $[1, 1, 1 \pm 0.103j]$

Parameter	Value	Unit
a	8.24	1/hour
b	50.9	1/hour^2
d	0.59	hour^2
dt	0.025	hour

Table 4.1: Simulation Parameters

Parameter	Value	Unit
η_{batt}	0.5	-
η_{panel}	0.1	-
A_{panel}	0.15	m^2
I_{sun}	1361	W/m^2
P_{load}	2	W
E_{max}	30	Wh

Table 4.2: Charging related parameters Parameters

Cooperative Target Vs. Non-cooperative Target

A comparison of case with and without target control is shown in Figures 4.2 and 4.3. In these cases, the initial condition of $-x_o$ is used since it is controllable in both scenarios. As shown in Figure 4.2a, in the non-cooperative (uncontrolled) target scenario, the chaser requires significantly more time (12.5 hours) to execute rendezvous compared to the case where target is cooperative(controllable) (4.07 hours) (Figure 4.2b). This obvious difference in the time to rendezvous can be attributed to better control authority in case of cooperative target and restricted control in case of non-cooperative target. Observing the control input for both the cases (Figure 4.3), it is evident how a cooperative control is leading to a shorter time to rendezvous using both chaser and target to achieve rendezvous. As seen in Figure 4.3b for first 2.5 hours, the chaser is in high drag mode($\theta \approx 90^\circ$) while target is in

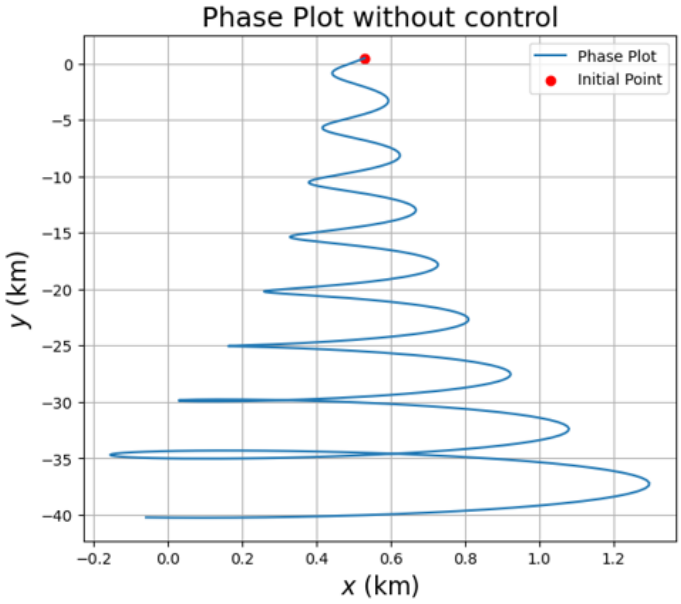

Figure 4.1: Phase Plot for uncontrolled case

low drag mode($\theta \approx 0°$). After this, the chaser goes into low drag mode, while target's drag increases for rendezvous operation. In non–cooperative case however (Figure 4.3a), chaser exerts control input for starting 2.5 hours, followed by almost 10 hours of coasting, using system dynamics to achieve rendezvous.

Figures 4.4 and 4.5 demonstrate shows that the relaxed optimization formulation produces solutions that adhere to the dynamics and constraints of the non-relaxed optimization problem. It is evident from Figure 4.5 that the constraint regarding the unit vector ($\|n(k)\| = 1$) is strictly followed in both the cases. Figure 4.4 shows that the relaxed dynamics is exactly following the equation from actual dynamics, $w(k) = \max(0, \nu(k))$. This illustrates the non-linear equation (3.7) for battery dynamics is exactly satisfied. In this case, the linear relaxation, does not cause any loss of information.

On-Off control Vs. Continuous Control

The minimum time to rendezvous is observed to be same for both the control approaches as mentioned in table 4.3, the simulation was carried out for a reduced d from (3.2). This

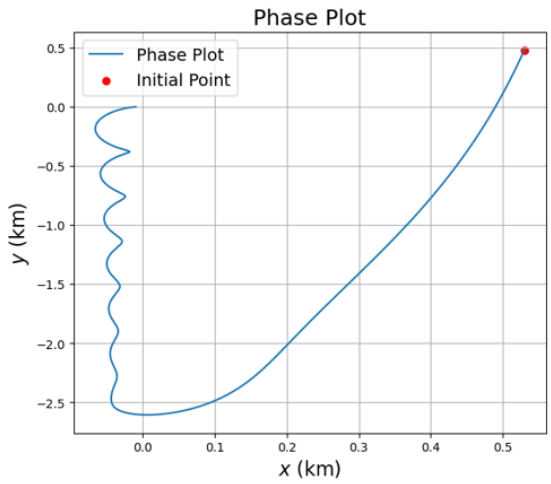

(a) When target is non-cooperative

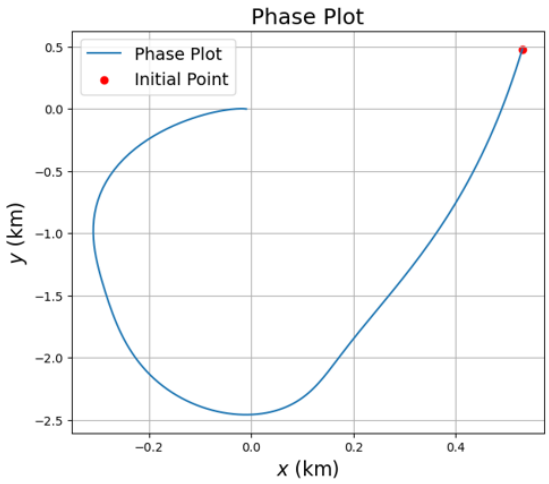

(b) When target is cooperative

Figure 4.2: Phase plots for the two cases

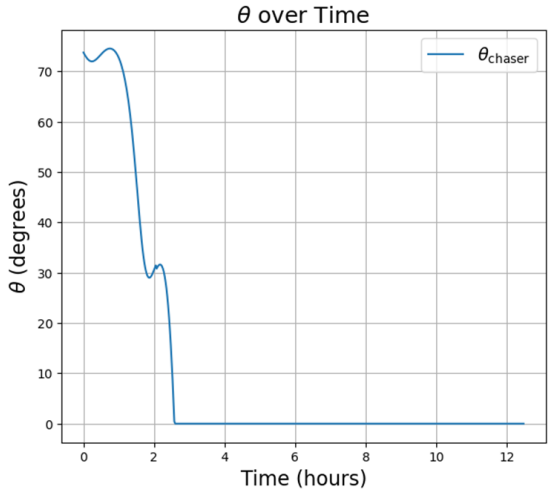

(a) When target is non-cooperative

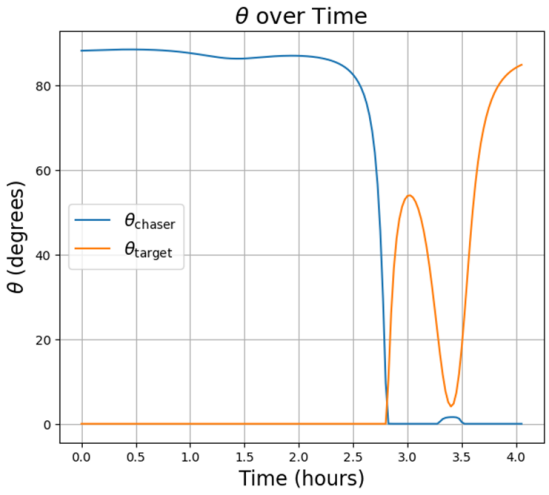

(b) When target is cooperative

Figure 4.3: Evolution of control input(θ) over time

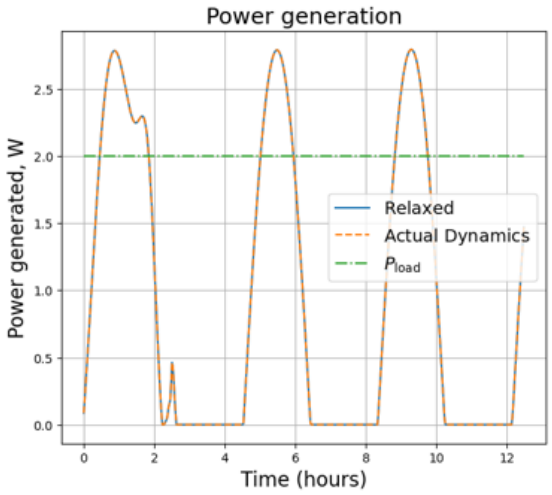

(a) When target is non-cooperative

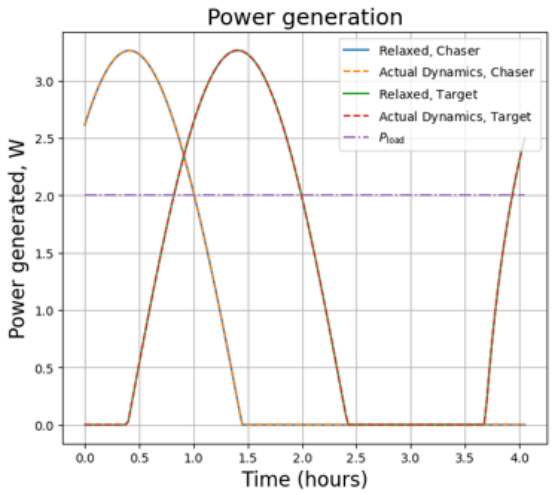

(b) When target is cooperative

Figure 4.4: Power generated with relaxed dynamics and actual dynamics

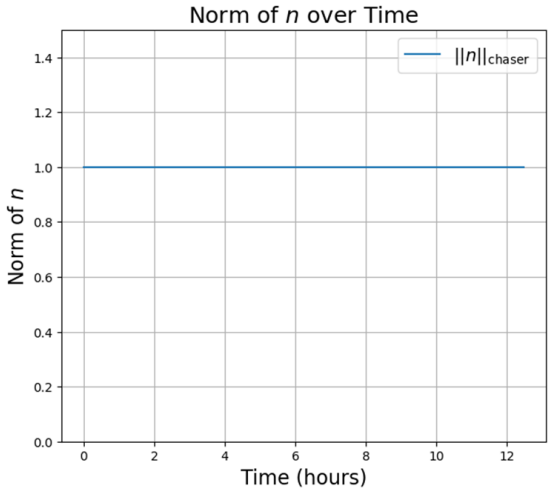

(a) When target is non-cooperative

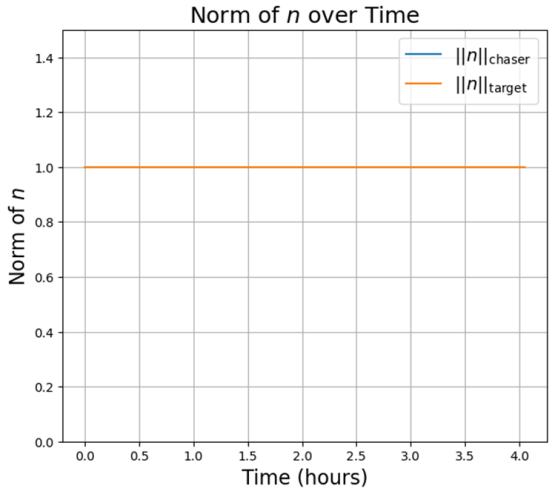

(b) When target is cooperative

Figure 4.5: Evolution of the norm of the unit vector $n(k)$ over time

situation simulates a scenario with lower atmospheric density, allowing the maneuver to last longer.

Although the times to rendezvous are identical, the phase plots in figure 4.6 show that evolution of state parameters are quite different in both cases, with increasing differences for longer mission duration. The continuous control follows a more gentle curve to rendezvous owing to smoother control as opposed to sudden On-Off control.

	$t_{\min}$ (hours)
$d' = d$	4.07
$d' = d/3$	13.3
$d' = d/5$	24.25

Table 4.3: Minimum time values

The general trend in control input is very similar in both cases (Figure 4.7a). For the first 2.5 hours, target is operated in maximum drag mode.($\theta \approx 90^\circ$ in case of continuous control and fully deployed in On-Off control). After 2.5 hours, Chaser's drag control is activated. When the two control inputs are scaled appropriately and overlaid on each other, as shown in the figure, a strong similarity between the two control schemes is observed, apart from the enforced discontinuous behavior of the On-Off controller. Similar trend is observed for other cases too in figure 4.8 and 4.9.

	Chaser		**Target**	
	Continuous	**On-Off**	**Continuous**	**On-Off**
$d' = d$	177.3°	450°	90.3°	450°
$d' = d/3$	570.4°	810°	60.4°	810°
$d' = d/5$	422.6°	1170°	809.6°	1170°

Table 4.4: Comparison of $\sum |\Delta\theta|$ Chaser and Target values

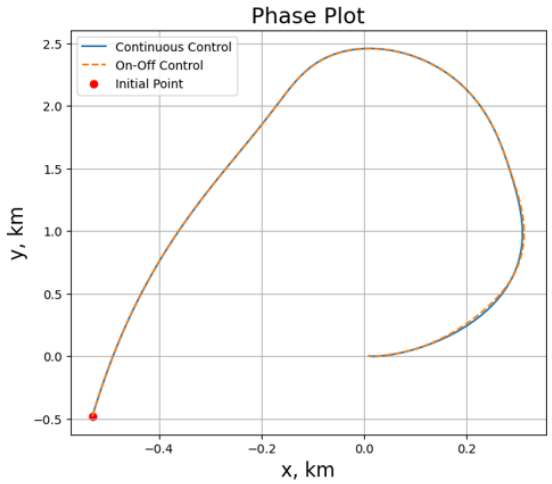

(a) Phase plot, ($d' = d$)

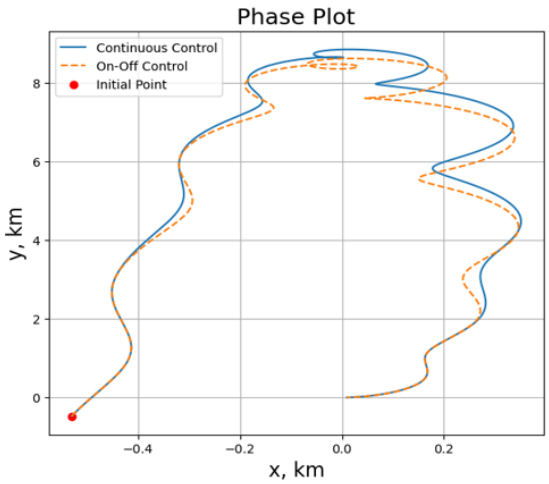

(b) Phase plot, ($d' = d/3$)

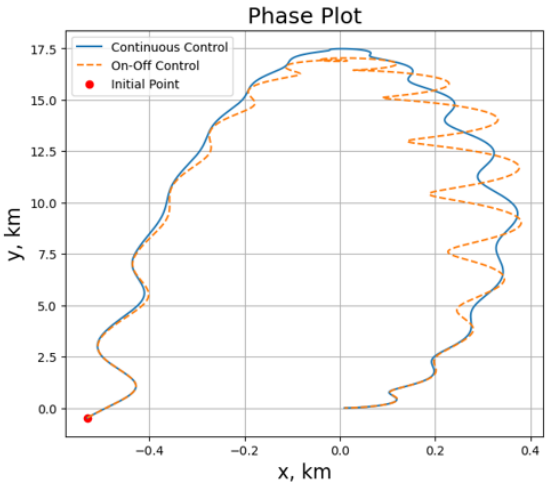

(c) Phase plot, ($d' = d/5$)

Figure 4.6: Phase plots for On-Off control and Continuous Control

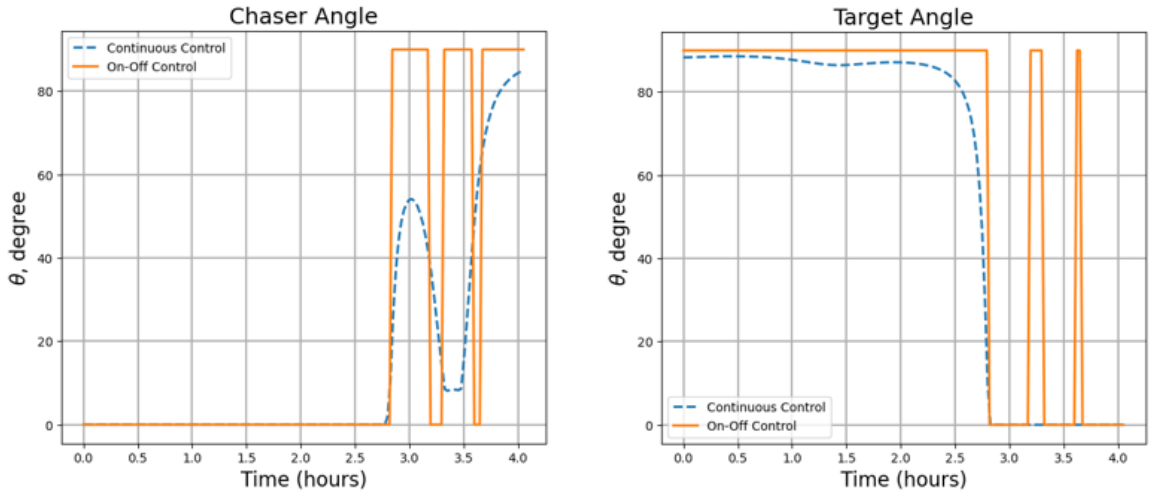

(a) Chaser control (b) Target Control

Figure 4.7: Comparison of control deployment for both the control schemes, for $d' = d$

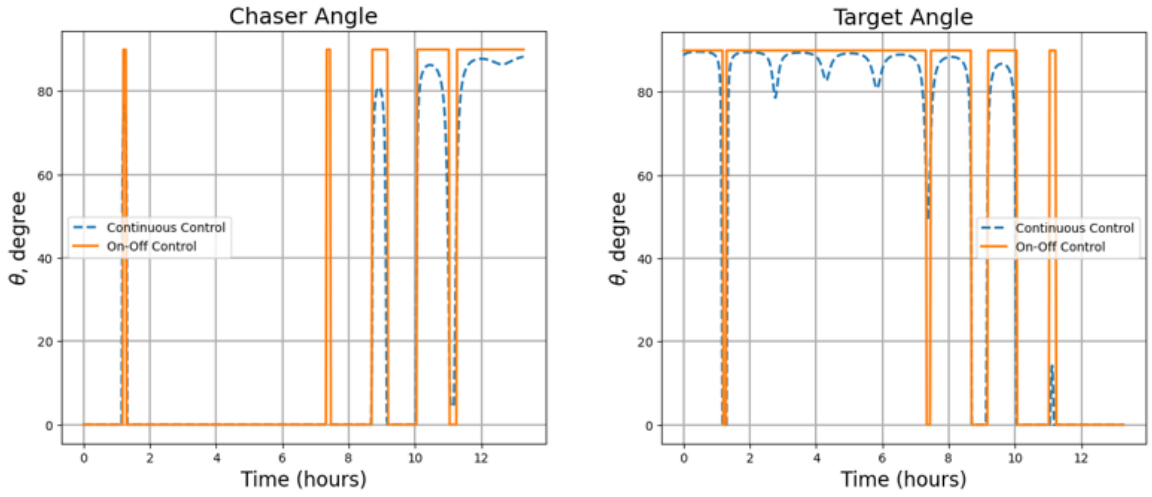

(a) Chaser control (b) Target Control

Figure 4.8: Comparison of control deployment for both the control schemes, for $d' = d/3$

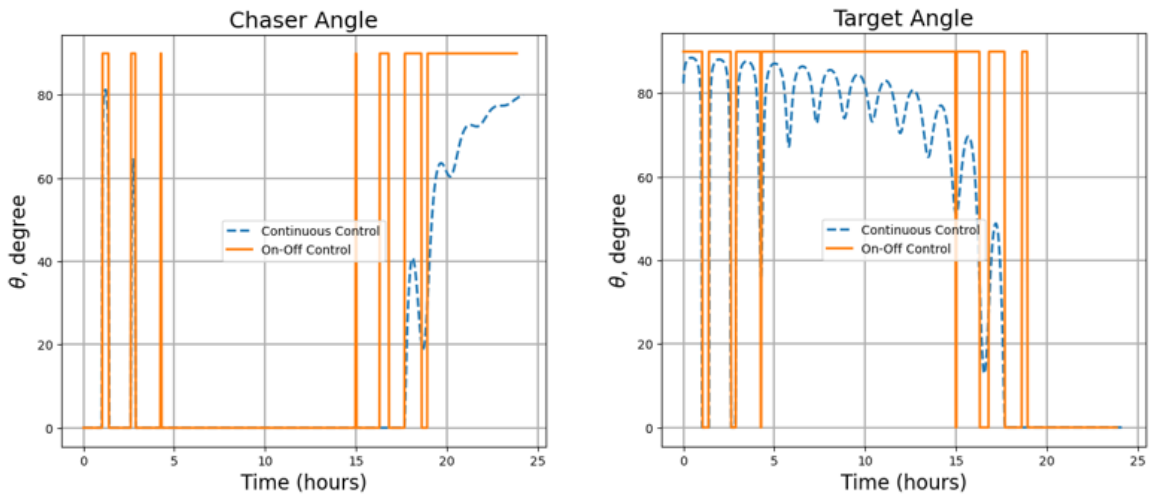

(a) Chaser control

(b) Target Control

Figure 4.9: Comparison of control deployment for both the control schemes, for $d' = d/5$

The amount of energy spent for control actuation at a given time is directly related to the absolute change in actuation angle, represented as $\sum |\Delta\theta|$, since a typical actuator for this kind of actuation uses energy only when moving(or changing angle). So, this quantity can be taken as a measure of control energy used throughout the mission. Table 4.4 lists this measure for the continuous and On-Off control. As evident from these numbers, for every maneuver, On-Off control is spending significantly higher energy compared to the continuous control. This is a major advantage in favour of continuous control scheme presented in this work.

Activation of the Battery SoC Constraint

So far, the constraint (3.8) associated with keeping the battery SoC above a certain level, is not explicitly utilized. Consider a case where, the solar panels' angle with respect to the body is fixed and cannot be controlled. For this fixed angle (θ), the dot product between the solar panels' normal unit vector and sun's unit vector is plotted in figure 4.10a. The figure contains cases where θ is fixed at 0° to 90° with 10° interval. Each of these cases exhibits

an identical trend in the dot product with a shift in X-axis, which can be interpreted as a lag.

The best a controller can do to maximize charging is to follow the element-wise maximum value of dot product at a given time. The angle θ which gives maximum dot product value at any time is plotted in figure 4.10b. So the best any controller could do is to track this plot. The product of α_d and the integral of the max curve (thick black curve) in Figure 4.10a gives us the measure of maximum amount of energy spacecraft can gain through solar panel by tracking θ_{max}. Let us denote the SoC at the end of such maneuver to be s_{best}. There is also a worst case scenario, where there is no charging available. Let us call the SoC at the end of this maneuver to be s_{worst}. If the $s_{min} > s_{best}$, it is not possible to keep the state of charge above the best possible case, hence this requirement will lead to infeasible solutions. It is possible that the optimal solution might still be feasible, since we are not enforcing exact dynamics, rather we are using a relaxed linear dynamics. In this case, the $w(k)$ will not follow the dynamics, $w(k) = \max(0, \nu(k))$ exactly. In fact, $w(k)$ will be greater than the maximum of 0 and $\nu(k)$, as shown in figures 4.12a and 4.12.

However, if s_{min} is less than s_{worst}, for any given scenario, $s(k) \geq s_{worst} > s_{min}$. That is at every time, the SoC is greater than s_{min} and the constraint is satisfied irrespective of the controller performance. With these restrictions, the designer is left with very little range of s_{min} to work with. Considering that these numbers do not account for the control input needed to stabilize, the actual feasible range is even lower. A typical set of numbers for a non-cooperative rendezvous operation is shown in table 4.5.

As demonstrated in table 4.5, while mathematically it is feasible to operate from almost 53% to 86%, we observe, with control and state constraint, actual range is just from 73.85% to 74%. Looking at figures 4.11 and 4.12, it is clear that if s_{min} is set higher than the observed feasibility, the $w(k)$ curve will simply lift above $\max(0, \nu(k))$ curve, which keeps it mathematically feasible, but not dynamically feasible.

To fully leverage the benefits of an Origami-based foldable solar panel, it is advantageous to incorporate multiple degrees of freedom into the solar panel through actuated hinges the $X - Y$ plane, which allows the solar panel more flexibility to align with the incoming solar rays and increase charging without affecting the controller performance.

Case	**s(N)**
Worst case	6.67
Nominal ($s_{min} = 0$)	44.45
$s_{min} = 45$	45
$s_{min} = 46$	Infeasible
$s_{min} = 50$	Infeasible
Best case	75.5(Infeasible)

Table 4.5: SoC at the end of maneuver for different cases

Optimizing Solar Efficiency with a Multi-Degree-of-Freedom Solar Panel

In this section, the results associated with solar panels with multi-degree-of-freedom are discussed. The case of uncooperative target from previous section is considered. In this case, the angle γ is bounded between $\pm\gamma_0$, and the value of γ_0 is 45°. This restricts solar panels from undergoing extreme actuation. It should be noted that, in this study, the occlusion of one panel due to other is not considered, which is a very likely possibility for the case when γ is allowed to be large. So, this restriction ensures that the assumption is not excessively violated.

Notice in figure 4.13d, the black line represents the boundary where the rate of charging is equal to rate of discharging, so if the dot products between the area vector of the solar panel and the sun unit vector is maintained above this level, there will be net increase in SoC otherwise SoC will decrease. In case of solar panel with single degree of freedom, due to restriction on movement of the panel, the ν curve crosses this threshold only three times for a relatively shorter duration, while the rest of the time, it is undergoing discharging. However, in case of panels with multi-degree-of-freedom, this value was consistently above the threshold and the spacecraft was always in charging mode. As a consequence of this, the state of charge in 2nd case never drops form initial level of 100%, as shown in figure 4.13a. This was made possible, due to extra degrees of freedom, which made it possible to align the solar panels in optimum direction while maintaining same effective projected area.

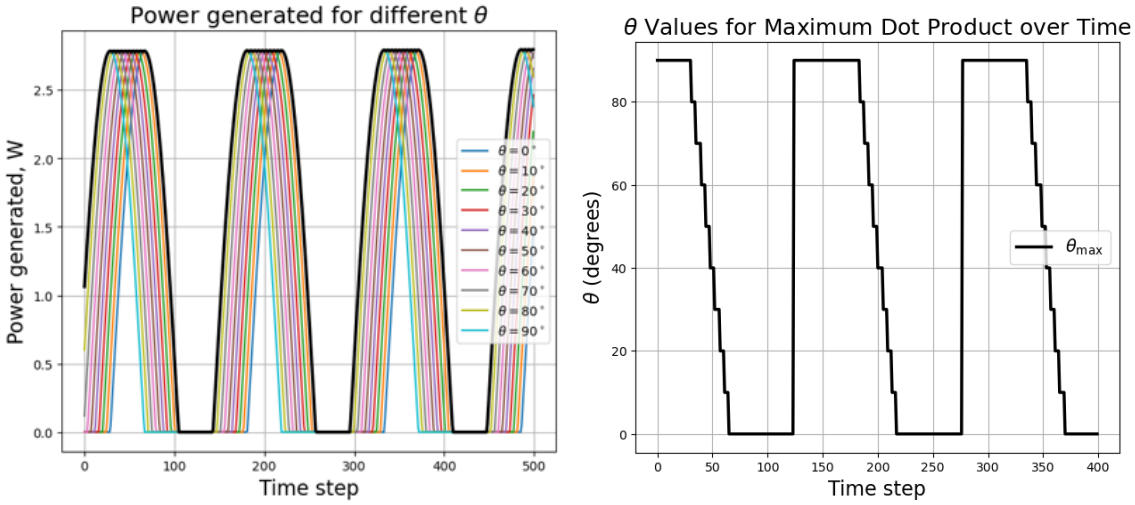

(a) Dot product between solar panel and sun unit vector

(b) Angle θ corresponding to maximum dot product

Figure 4.10: Condition for maximum charging

As shown in figure 4.13b, angle θ for 3DOF case adjusts to compensate for the projected area lost due to angle γ (shown in figure 4.13c) of the panels on the side. Note this angle $\theta_{3 \text{ Degree of Freedom}}$ is actually θ_f from (3.23).

4.2 Origami Control

The schematic used for modeling the deployment and control of the solar panels in the spacecraft is shown in figure 4.14. There are 5 solar panels of 10×30 cm^2 area each, connected along a hinge along the longer edge. The central panel is connected to the body along the shorter edge. In this study, actuation is applied solely to the hinge connecting the solar panels to the spacecraft. As evident from the figure, the N4B5 configuration is used for modeling the panels, i.e., each panel is represented by 4 particles places on the vertices and a single pair of diagonal particles are connected with a bar and a bending hinge. In figure 4.14, the green edges represent a bending hinge, and a red edge represents a folding hinge.

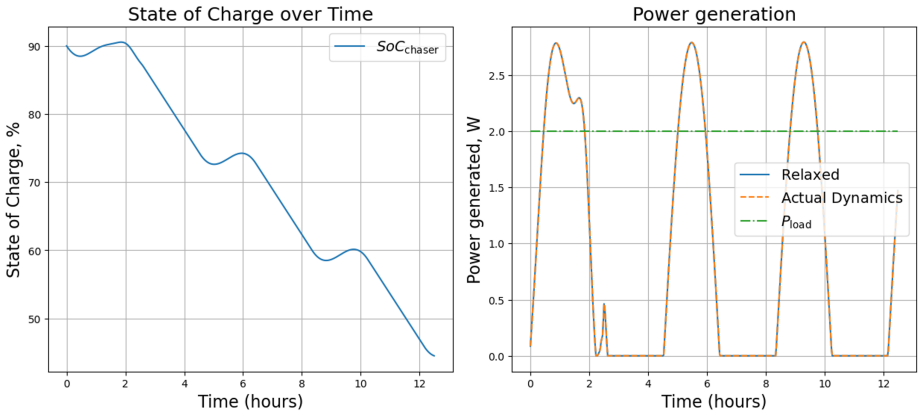

(a) Data for $s_{min} = 0\%$ case

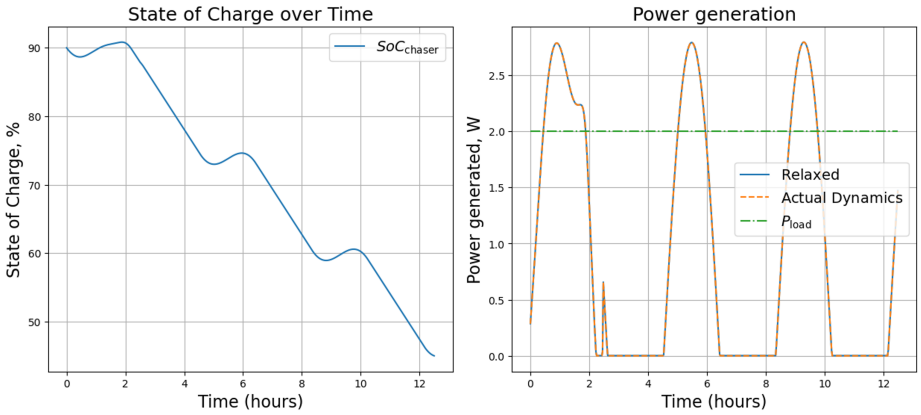

(b) Data for $s_{min} = 45\%$ case

Figure 4.11: SoC data for different s_{min} cases

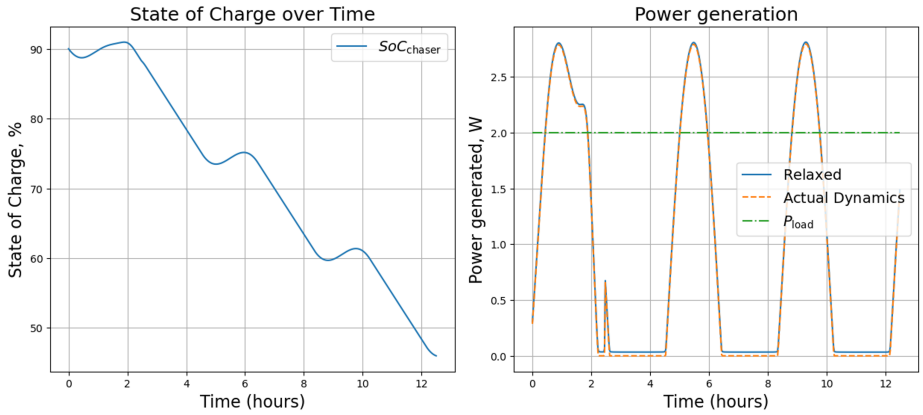

(a) Data for $s_{min} = 46\%$ case

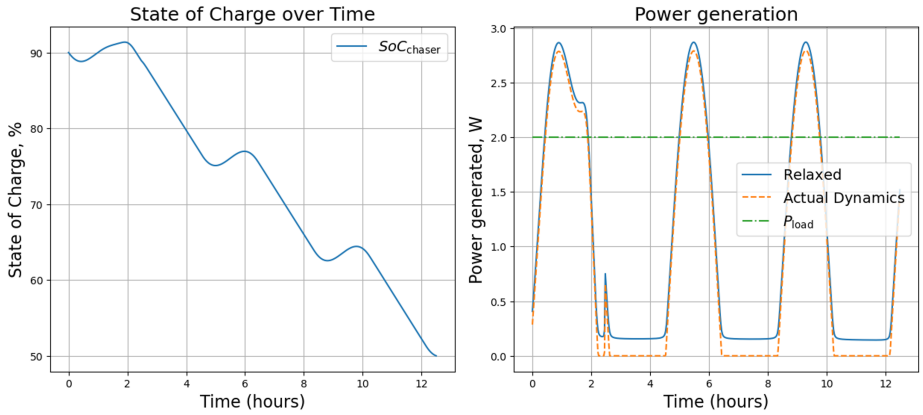

(b) Data for $s_{min} = 50\%$ case

Figure 4.12: SoC data for different s_{min} cases (figure continued)

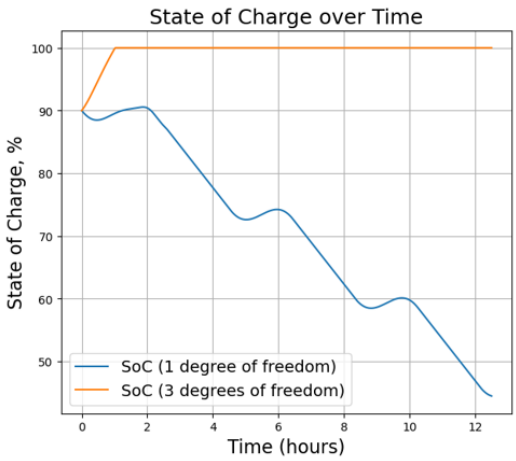

(a) State of Charge, (%)

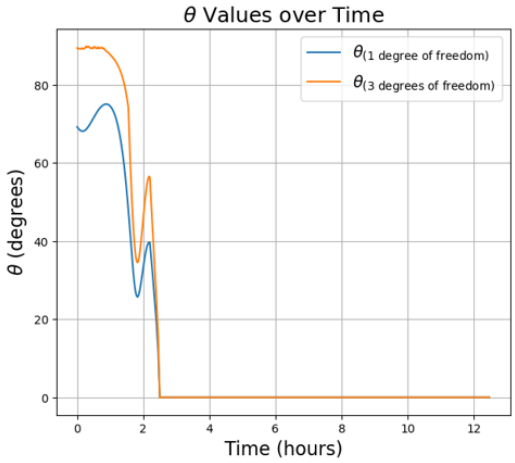

(b) Angle θ, (°)

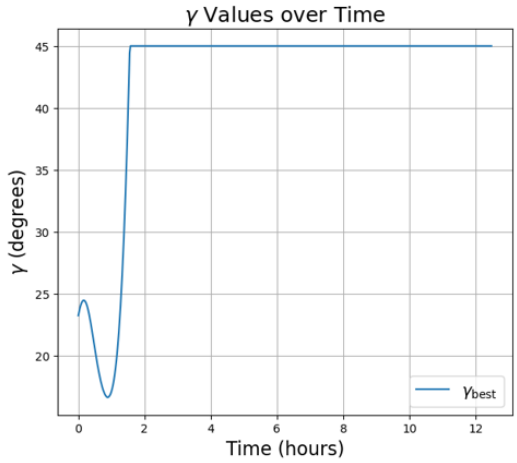

(c) Angle γ, (°)

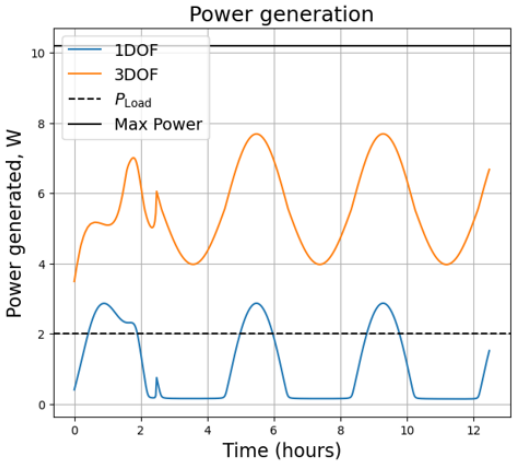

(d) Power generated

Figure 4.13: Comparison of fixed panels and 3 degree of freedom panels

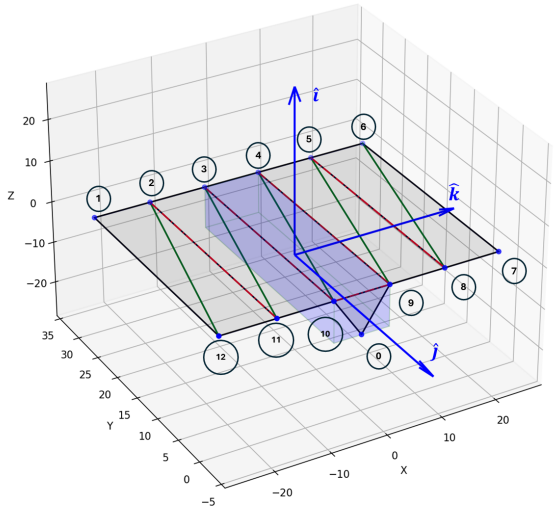

Figure 4.14: Schematic of the Origami model of the spacecraft with solar panels

All the folding edges, except edge $\{9, 10\}$, have neutral angle of 180°, which means under no force, the panels will be totally flat, the neutral angle for edge $\{9, 10\}$ is 90°, which is for reliability purpose. In case of power failure, the satellite will go into the least drag condition. The stiffness per unit length(K^F) for edges $\{2, 11\}$ and $\{5, 8\}$ is $0.1N$/deg. For edges $\{3, 10\}$ and $\{4, 9\}$, the stiffness is twice that of the other two edges. This was done to ensure similar opening times from fully deployed condition for both the edges. As shown in figure 4.15, under stowed condition, the folding angle for edge $\{2, 11\}$ is almost 0° whereas for edge $\{3, 10\}$, it is 90°. So for same stiffness, particles associated with the former edge will experience greater force(almost double), leading to that edge flattening out faster than inner edge. By increasing the stiffness of the inner edge, the aim is to achieve similar deployment times for both the edges.

Bending stiffness per unit length is $10000N$/deg. Other material properties are, the Modulus of elasticity is $1.2 \times 10^5 N/\text{cm}^2$, Poisson' ratio is 1/3 and density is 1.76Kg/m^2 for the thickness of 5.5cm. The damping factor is 100.

A simple Proportional-Integral-Derivative(PID) control is implemented to control the angle θ for drag area modulation. Note that this angle θ is the folding angle for the folding

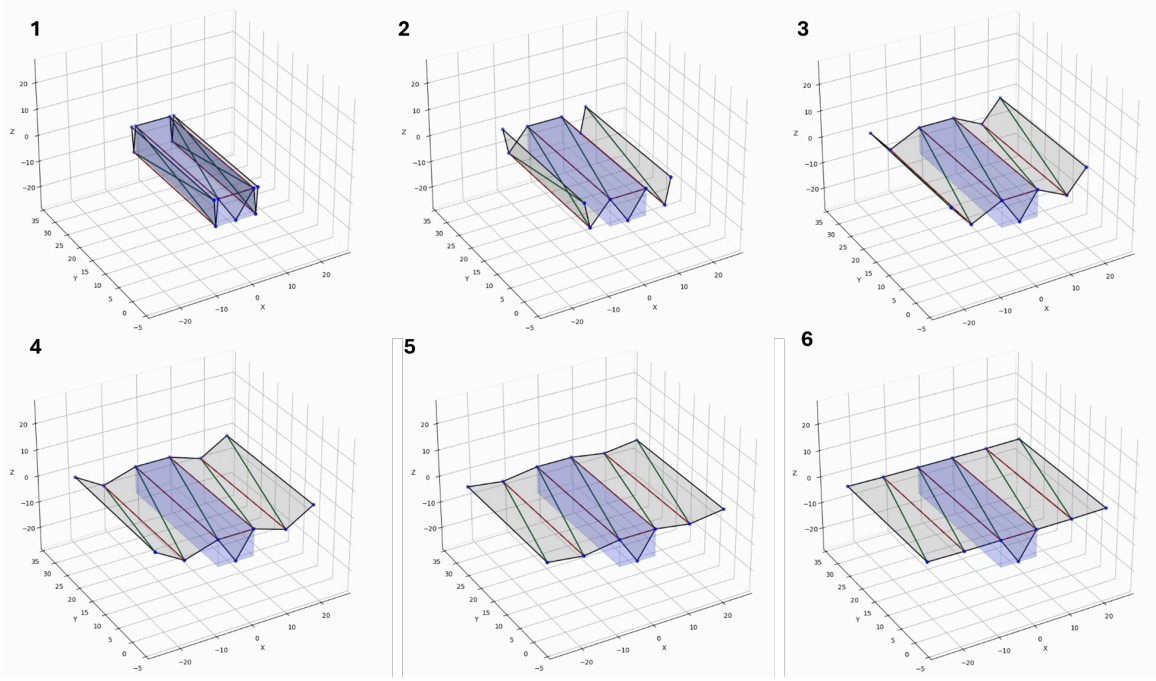

Figure 4.15: Deployment of Solar Panels from stowed condition

hinge, $\{9, 10\}$. The control input is the torque at the hinge.

In figure 4.16, the response of the system to a PID control input, with $(K_P, K_I, K_D) = (10, 0.5, 0.5)$ is plotted. The controlled folding angle is plotted on the left while the uncontrolled angles are shown on the right. It can be observed that the individual inertia of each solar panel contributes to folding at the uncontrolled hinges as well. This folding/flexing then hinders the performance of the controller, since additional forces are exerted on the panels. To limit the flexing, the reference input rate is controlled, i.e., the input is a ramp function as opposed to a step function. As shown in figures 4.17 and 4.18, with a ramp input, the flex in the panels is minimized. Additionally, with ramp input, the overshoot is lesser even with a higher proportional term K_P and a lower derivative term K_D. The overshoot is a major concern especially when the panel angle is commanded to zero, as an overshoot will cause the panel to hit the surface of the satellite, cause other hardware issues, along with extra flexing of the panels.

To determine the maximum value of allowable $\dot{\theta}$, the case of minimum time rendezvous

for cooperative target configuration is referred. The variation of $\dot{\theta}(t)$ with time t is shown in figure 4.19. As per this figure, the maximum observed value of $\dot{\theta}$ is around 0.2deg/sec. For the controller design, a $\dot{\theta}$ value of 0.25 is considered. For a given desired angle θ_{des}, current angle θ_{current} and maximum allowable $\dot{\theta}$, the reference θ_{ref} at time t is given as,

$$\begin{aligned}\theta_{\text{ref}}(0) =& \theta_{\text{current}} \\ \theta_{\text{ref}}(t) =& \theta_{\text{ref}}(t-1) + \dot{\theta} \times dt\end{aligned}$$

When θ_{ref} is close enough to θ_{des}, we set,

$$\theta_{\text{ref}} = \theta_{\text{des}}$$

It should also be noted that if, θ_{ref} is consistently not equal to θ_{des}, a persistent error accumulates over time, causing integral windup issues in practical cases and degrading control accuracy. So some kind of remedy for integral windup has to be included in the current controller. In current case, the integral errors are reset to zero reference gets close to the desired angle.

Final design parameters(response shown in figure 4.20),

$$\dot{\theta} = 0.25\text{deg/sec}, K_P = 50, K_I = 5, K_D = 0.01$$

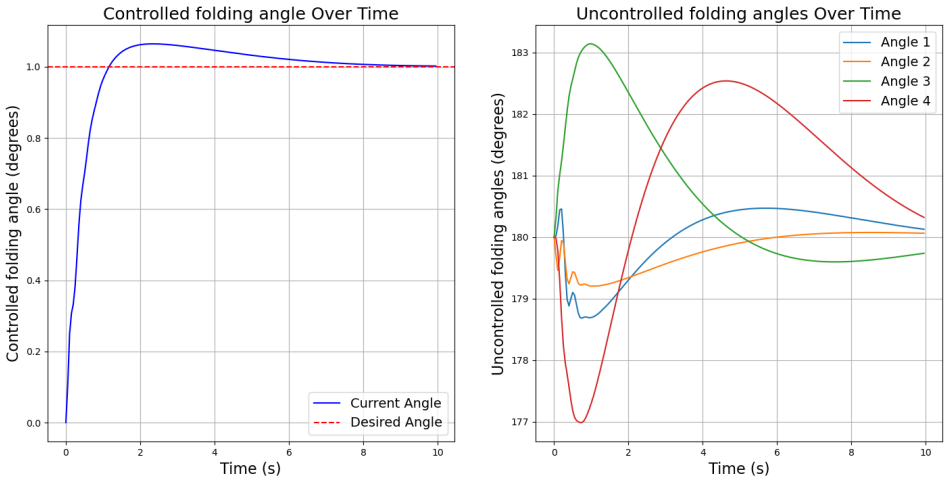

Figure 4.16: PID $K_P = 10, K_I = 0.5, K_D = 0.5$

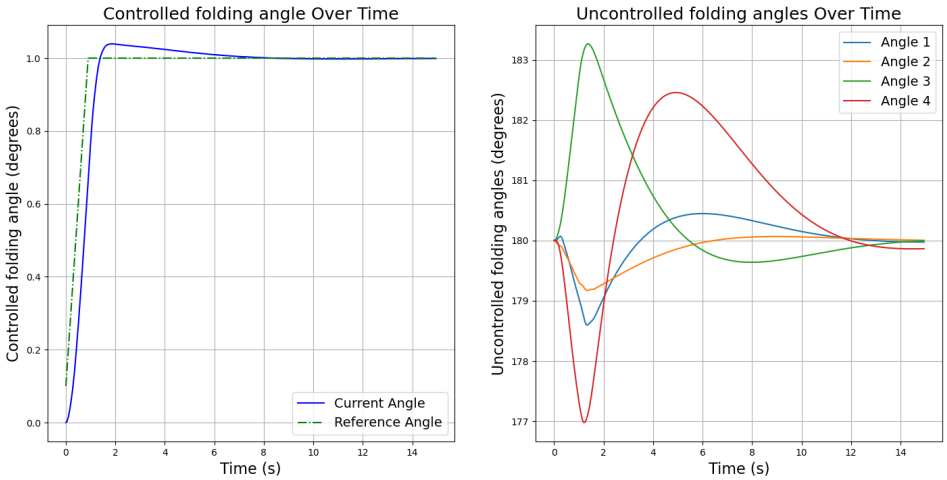

Figure 4.17: PID $K_P = 15, K_I = 0.1, K_D = 0.01, \dot{\theta} = 1\text{deg/sec}$

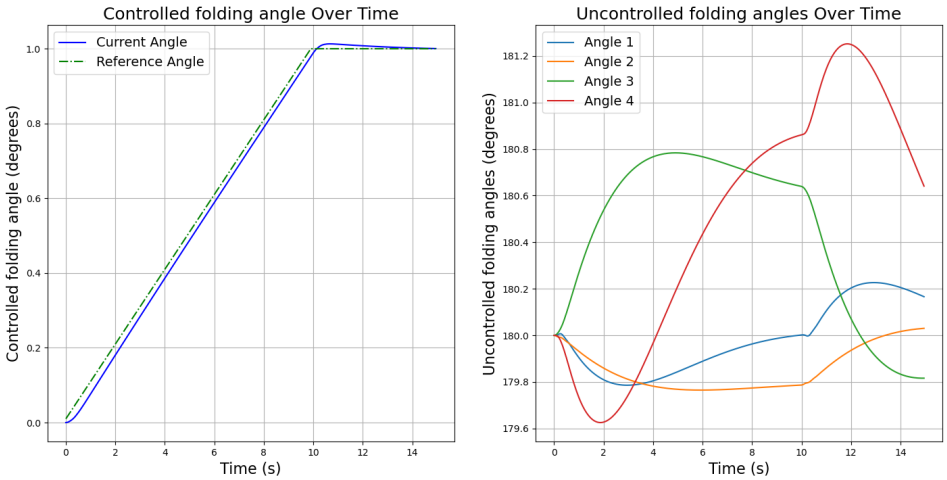

Figure 4.18: PID $K_P = 15, K_I = 0.1, K_D = 0.01, \dot{\theta} = 0.1\text{deg/sec}$

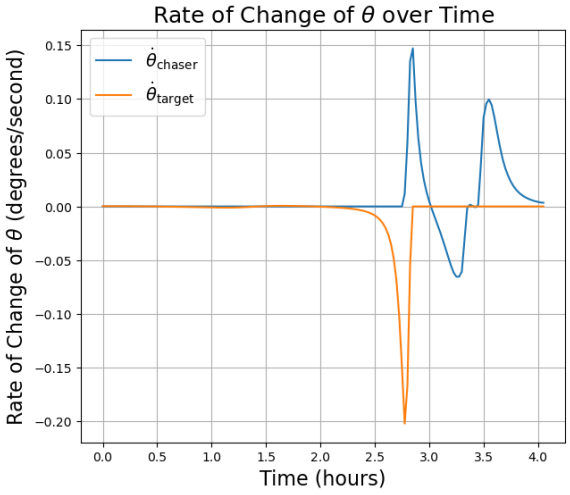

Figure 4.19: Rate of change of θ for minimum time case

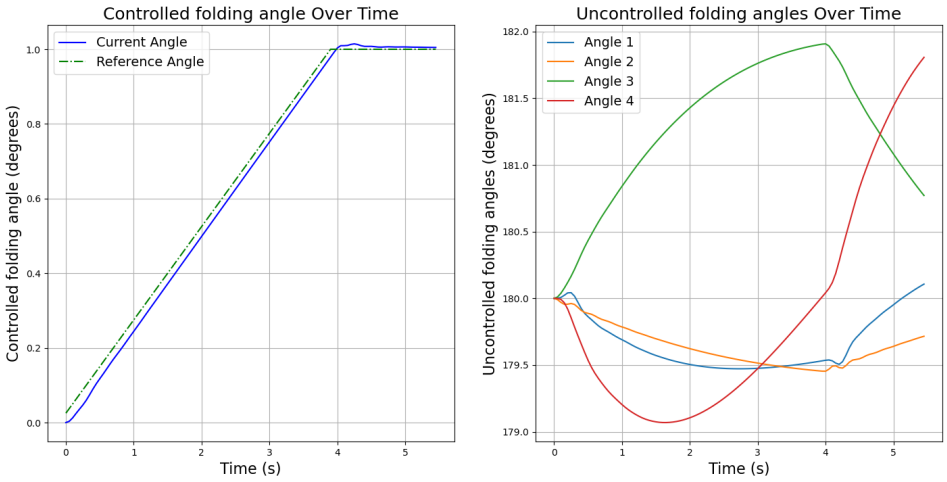

Figure 4.20: PID $K_P = 50, K_I = 5, K_D = 0.01, \dot{\theta} = 0.25\text{deg/sec}$

Chapter 5

CONCLUSIONS

Over the last two decades, there has been a remarkable surge in the number of small satellites in orbit in the form of Nanosats and Cubesats. This surge is propelled by relatively low launch costs and readily available commercial-off-the-shelf components. Many of these satellites aim to minimize, even eliminate the chemical propellants in favor of differential drag for relative orbital maneuvers. There are several missions which accomplished it with a great deal of operational efficiency. However, the way it is done in almost every case restricts this control method to be used in On-Off mode, which limits this approach's potential. Another recent technological advancement is the use of Origami based space structures, which allow large structures be be stowed in small confines of the launch vehicle payload bay and deployed in space. The current work aims to take advantages of both these approaches to come up with a system which increases the efficiency of differential drag based control using origami-based structures.

To achieve this, the thesis first investigates the high level control and guidance algorithm for rendezvous operations between two identical satellites operating in Low Earth Orbit (LEO). In this part, the relative dynamics are considered in the form of linear Schweighart-Sedwick equations. The time optimal rendezvous operation is formulated as a discrete optimization problem with a non-convex, non-linear constraint associated with the unit vector and the non-linear battery charging dynamics which was handled through a slack variable. The unit vector constrained was first expressed as a non-linear function and then linearized around a reference point. The corresponding optimal control problem was then solved sequentially. The minimum time was obtained using a bisection method to find a feasible solution to the discrete optimal control problem. The results were compared for a non-cooperative target case and a cooperative target case, which showed a great deal of difference in optimal control times, particularly in scenarios where non-cooperative control

successfully stabilized the system (successfully execute rendezvous). This control scheme was compared with the On–Off control method and was found to achieve the same minimum rendezvous time. However, its state evolution was noticeably smoother. Furthermore, an evaluation of energy consumption during actuation revealed that continuous control provides significantly greater energy savings while delivering equivalent performance. The practical effectiveness of the battery charge constraint was investigated and it was concluded that, to fully capitalize on this method, more degrees of freedom are needed, i.e., a more articulated origami structure. Finally, a simple approach to improve charging performance using a solar panel with two additional degrees of freedom was proposed. This approach further complicates the optimal control problem, due to non-linear, non-convex constraints associated with the normal vectors for each panel. This problem is tackled by solving the optimal control problem assuming fixed panels (single degree of freedom), then additional two degrees of freedom are used to optimize solar exposure without affecting the trajectory and control inputs obtained from the optimal control problem. In a sample example, it was observed that the spacecraft was generating power throughout the maneuver using actuated solar panels.

Subsequently, the lower-level control design was investigated. The solar panel was modeled as a foldable origami structure. A simple PID control was designed to control the angle θ between the solar panel and the body of the spacecraft. To reduce flexing of the solar panels, the rate of change of angle θ was restricted to 0.25deg/sec based on worst-case observations from minimum time rendezvous problem. The reference angle is first calculated based on current angle, desired angle and maximum allowed rate of change of angle. Given these parameters, rotating the panel from 0° to 90° is expected to be completed in over six minutes, which is reasonable considering the outer control loop operates at a slower pace, typically spanning several hours.

In summary, by integrating the origami based structure with differential drag, this work demonstrates how propulsion-less spacecraft can execute precise and efficient maneuvers.

5.1 Future Efforts

This study lays a solid foundation for exploring interesting problems in the domain of origami-based spacecraft maneuvering and control. The following avenues present significant opportunities:

- Exploring formation-keeping maneuvers: As discussed in the results and conclusions, the true advantage of continuous control becomes evident when maneuvers take a considerable amount of time. Formation-keeping falls into this category of maneuvers, some of which may last for days. Important mission aspects such as initial phasing, maintaining constant relative separation, and collision avoidance strategies can be thoroughly analyzed.

- Additional constraints related to mission requirements: In this study, only constraints related to battery state of charge were considered. However, many other mission-critical constraints can be explored and incorporated into the problem formulation. One important constraint could be to minimize altitude loss during the maneuver, to ensure long-term mission efficiency and sustainability. Other constraints related to pointing, due to communication or imaging requirements, can also be incorporated.

- Mathematically rigorous incorporation of origami structures into the problem statement: This approach will allow for a true understanding and utilization of highly articulated structures in the problem formulation for various mission scenarios.

BIBLIOGRAPHY

[1] Erik Kulu. Cubesats & nanosatellites - 2024 statistics, forecast and reliability. In *Proceedings of the 75th International Astronautical Congress*, Milan, Italy, 2024. International Astronautical Federation (IAF).

[2] Shuqin Dong, Xiaohua Zhao, and Ying Yu. Dynamic unfolding process of origami tessellations. *International Journal of Solids and Structures*, 226-227:111075, 2021.

[3] Avishai Weiss, Uroš V. Kalabić, and Stefano Di Cairano. Station keeping and momentum management of low-thrust satellites using mpc. *Aerospace Science and Technology*, 76:229–241, 2018.

[4] Planet labs inc., our constellations. https://www.planet.com/our-constellations/.

[5] Joseph W. Gangestad, Brian S. Hardy, and David A. Hinkley. Operations, orbit determination, and formation control of the aerocube-4 cubesats. In *27th Annual AIAA/USU Conference on Small Satellites*, Logan, UT, 2013. AIAA/USU.

[6] Cyrus Foster, Henry Hallam, and James Mason. Orbit determination and differential-drag control of planet labs cubesat constellations. *arXiv*, 2015.

[7] Cyrus Foster, James Mason, Vivek Vittaldev, Lawrence Leung, Vincent Beukelaers, Leon Stepan, and Rob Zimmerman. Differential drag control scheme for large constellation of planet satellites and on-orbit results. *arXiv*, 2018.

[8] C. S. Ruf, C. Chew, T. Lang, M. G. Morris, K. Nave, A. Ridley, and R. Balasubramaniam. A new paradigm in earth environmental monitoring with the CYGNSS small satellite constellation. *Scientific Reports*, 8(1):8782, 2018.

[9] Scott Hull, Amanda Shelton, and David Richardson. Differential drag demonstration: A post-mission experiment with the eo-1 spacecraft. In *1st IAA Conference on Space Situational Awareness*, Orlando, FL, 2017. International Academy of Astronautics.

[10] C. L. Leonard. Formationkeeping of spacecraft via differential drag. *M.Sc. Thesis, Massachusetts Int. of Technology, Cambridge, MA*, July, 1986.

[11] C. L. Leonard, W. M. Hollister, and E. V. Bergmann. Orbital formationkeeping with differential drag. *Journal of Guidance, Control, and Dynamics*, 12(1):108–113, 1989.

[12] B.S. Kumar and A. Ng. A bang-bang control approach to maneuver spacecraft in a formation with differential drag. In *Proceedings of the AIAA Guidance, Navigation and Control Conference and Exhibit*, pages 1–11, Honolulu, Hawaii, 2008.

[13] R. Bevilacqua and M. Romano. Rendezvous maneuvers of multiple spacecraft using differential drag under j2 perturbation. *Journal of Guidance, Control, and Dynamics*, 31(6):1595–1607, 2008.

[14] Samuel A. Schweighart and Raymond J. Sedwick. High-fidelity linearized j model for satellite formation flight. *Journal of Guidance, Control, and Dynamics*, 25(6):1073–1080, 2002.

[15] R. Bevilacqua, J.S. Hall, and M. Romano. Multiple spacecraft rendezvous maneuvers by differential drag and low thrust engines. *Celestial Mechanics and Dynamical Astronomy*, 106:69, 2010.

[16] Matthew W. Harris and Behçet Açıkmeşe. Minimum time rendezvous of multiple spacecraft using differential drag. *Journal of Guidance, Control, and Dynamics*, 37(2):365–373, 2014.

[17] D. Pérez and R. Bevilacqua. Lyapunov-based spacecraft rendezvous maneuvers using differential drag. In *AIAA Guidance, Navigation, and Control Conference*, Portland, Oregon, 2011.

[18] L. Dell'Elce, V. Martinusi, and G. Kerschen. Robust optimal rendezvous using differential drag. In *AIAA/AAS Astrodynamics Specialist Conference*, San Diego, CA, USA, 2014.

[19] C. Lambert, B. S. Kumar, J.-F. Hamel, and A. Ng. Implementation and performance of formation flying using differential drag. *Acta Astronautica*, 71:68–82, 2012.

[20] L. Dell'Elce and G. Kerschen. Propellantless rendez-vous of qb-50 nanosatellites. In *63rd International Astronautical Congress*, Naples, Italy, 2012.

[21] L. Dell'Elce and G. Kerschen. Validation of differential drag propellantless maneuvers using 6dof simulations and stochastic dynamics. In *9th International ESA Conference on Guidance, Navigation and Control*, Oporto, Portugal, 2014.

[22] L. Dell'Elce and G. Kerschen. Orbital rendez-vous using differential drag in the qb50 constellation. In *AIAA/AAS Astrodynamics Specialist Conference*, Minneapolis, Minnesota, 2012.

[23] L. Dell'Elce and G. Kerschen. Optimal propellantless rendez-vous using differential drag. *Acta Astronautica*, 109:112–123, 2015.

[24] R. Twiggs, B. Malphrus, and J. Muylaert. The qb50 program, the first cubesat constellation doing science. In *24th Annual AIAA/USU Conference on Small Satellites*, Logan, Utah, 2010.

[25] D. Pérez and R. Bevilacqua. Spacecraft maneuvering via atmospheric differential drag using an adaptive lyapunov controller. In *Advances in the Astronautical Sciences*, volume 148, pages 3855–3874, 2013.

[26] R. Bevilacqua. Analytical guidance solutions for spacecraft planar rephasing via input shaping. *Journal of Guidance, Control, and Dynamics*, 37(3):1042–1047, 2014.

[27] R. Bevilacqua and T.A. Lovell. Analytical guidance for spacecraft relative motion under constant thrust using relative orbit elements. *Acta Astronautica*, 102:47–61, 2014.

[28] M. Pastorelli, R. Bevilacqua, and S. Pastorelli. Differential-drag-based roto-translational control for propellant-less spacecraft. *Acta Astronautica*, 114:6–21, 2015.

[29] D. Spiller, F. Curti, and C. Circi. Minimum-time reconfiguration maneuvers of satellite formations using perturbation forces. *Journal of Guidance, Control, and Dynamics*, 40(5):1130–1143, 2017.

[30] M. Mathews and S.J. Leszkiewicz. Efficient spacecraft formation-keeping with consideration of ballistic coefficient control. In *26th Aerospace Science Meeting*, Reno, NV, USA, 1988.

[31] Jean Fourcade. Mission analysis and orbit control of interferometric wheel formation flying. In *18th International Symposium on Space Flight Dynamics*, Munich, Germany, 2004.

[32] H. Jigang and Z. Yulin. Application of phase-plane method in the co-plane formation maintenance of formation flying satellites. In *2006 Chinese Control Conference*, pages 1900–1904, Harbin, China, 2006. IEEE.

[33] J. T. Wedekind. Characterizing and controlling the effects of differential drag on satellite formations. Master's thesis, Air Force Institute of Technology, 2006.

[34] B. S. Kumar, A. Ng, K. Yoshihara, and A. de Ruiter. Differential drag as a means of spacecraft formation control. In *2007 IEEE Aerospace Conference*, Big Sky, MT, USA, 2007. IEEE.

[35] F. Bellefeuille. Satellite formation maintenance using differential atmospheric drag. Master's thesis, McGill University, 2011.

[36] T. Reid and A. K. Misra. Formation flight of satellites in the presence of atmospheric drag. *Journal of Aerospace Engineering, Science and Applications*, 3(1), 2011.

[37] G. Zeng, M. Hu, and H. Yao. Relative orbit estimation and formation keeping control of satellite formations in low earth orbits. *Acta Astronautica*, 76:164–175, 2012.

[38] James R. Clark and Dolan E. Highsmith. Decision aid for conjunction risk mitigation by differential drag. In *Proceedings of the AAS/AIAA Space Flight Mechanics Meeting*, page 20240015015, Kaua'i, Hawaii, January 2025. American Institute of Aeronautics

and Astronautics and American Astronautical Society, NASA Goddard Space Flight Center. NASA Contract Grant: 80GSFC19D0011.

[39] Andreas Fanebust. Satellite formation flying using attitude-controlled differential drag. Master's thesis, Norwegian University of Science and Technology (NTNU), Trondheim, Norway, October 2024. Available at NTNU Library: https://hdl.handle.net/11250/3158608.

[40] James webb space telescope. https://science.nasa.gov/mission/webb/.

[41] Project starshade. https://exoplanets.nasa.gov/exep/technology/starshade/.

[42] Mark Schenk and Simon D. Guest. Origami folding: A structural engineering approach. 2011.

[43] E.T. Filipov, K. Liu, T. Tachi, M. Schenk, and G.H. Paulino. Bar and hinge models for scalable analysis of origami. *International Journal of Solids and Structures*, 124:26–45, 2017.

[44] Koryo Miura. Zeta-core sandwich-its concept and realization. *ISAS report/Institute of Space and Aeronautical Science,University of Tokyo*, 37(6):137–164, 05 1972.

[45] Liu K. and Paulino G.H. Nonlinear mechanics of non-rigid origami: an efficient computational approach. *Proc. R. Soc.*, 2017.

Appendix A

COORDINATE FRAMES TRANSFORMATION

The relative position $\mathbf{r}$ and velocity $\dot{\mathbf{r}}$ in inertial frame is defined first. We use superscript I for inertial and R for rotating frame.

$$\mathbf{r}^I = \mathbf{r}_c^I - \mathbf{r}_t^I \tag{A.1}$$

$$\dot{\mathbf{r}}^I = \dot{\mathbf{r}}_c^I - \dot{\mathbf{r}}_t^I \tag{A.2}$$

The transformation from the inertial frame to rotating frame is given by,

$$\mathbf{r}^R = C\mathbf{r}^I \tag{A.3}$$

$$\mathbf{r}^R = \dot{C}\mathbf{r}^I + C\dot{\mathbf{r}}^I \tag{A.4}$$

Similarly the transform from rotational frame to the inertial frame is given by,

$$\mathbf{r}^I = C^T\mathbf{r}^R \tag{A.5}$$

$$\mathbf{r}^I = \dot{C}^T\mathbf{r}^R + C^T\dot{\mathbf{r}}^R \tag{A.6}$$

Now, we need to derive C and $\dot{C}$. We start by defining the axes for fixed frame as $[\hat{I}, \hat{J}, \hat{K}]$ and rotating frame as $[\hat{e}_x, \hat{e}_y, \hat{e}_z]$ as shown in Figure A.1. Where:

$$\hat{e}_x = \hat{e}_{x_i}\hat{I} + \hat{e}_{x_j}\hat{J} + \hat{e}_{x_k}\hat{K} \tag{A.7}$$

$$\hat{e}_y = \hat{e}_{y_i}\hat{I} + \hat{e}_{y_j}\hat{J} + \hat{e}_{y_k}\hat{K} \tag{A.8}$$

$$\hat{e}_z = \hat{e}_{z_i}\hat{I} + \hat{e}_{z_j}\hat{J} + \hat{e}_{z_k}\hat{K} \tag{A.9}$$

$$\tag{A.10}$$

With this definition,

$$C = \begin{bmatrix} (\hat{e}_x \cdot \hat{I}) & (\hat{e}_x \cdot \hat{J}) & (\hat{e}_x \cdot \hat{K}) \\ (\hat{e}_y \cdot \hat{I}) & (\hat{e}_y \cdot \hat{J}) & (\hat{e}_y \cdot \hat{K}) \\ (\hat{e}_z \cdot \hat{I}) & (\hat{e}_z \cdot \hat{J}) & (\hat{e}_z \cdot \hat{K}) \end{bmatrix} = \begin{bmatrix} \hat{e}_{x_i} & \hat{e}_{x_j} & \hat{e}_{x_k} \\ \hat{e}_{y_i} & \hat{e}_{y_j} & \hat{e}_{y_k} \\ \hat{e}_{z_i} & \hat{e}_{z_j} & \hat{e}_{z_k} \end{bmatrix} \tag{A.11}$$

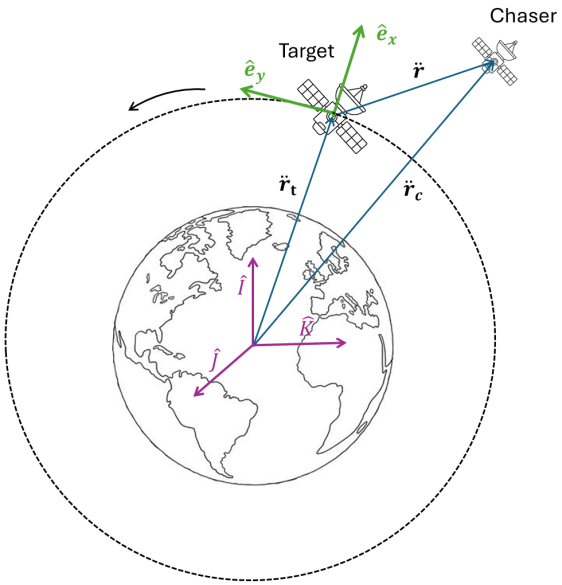

Figure A.1: Vector diagram depicting the relation between different coordinate frames

and the transformation matrix derivative is

$$\dot{C} = \frac{d}{dt}C \tag{A.12}$$

For Hill's frame, basis vectors are defined as

$$\hat{e}_x = \hat{\mathbf{r}}_t \tag{A.13}$$

$$\hat{e}_z = \hat{\mathbf{h}}_t \tag{A.14}$$

$$\hat{e}_y = \hat{e}_z \times \hat{e}_x \tag{A.15}$$

$$\tag{A.16}$$

Now we need the derivatives,

$$\begin{aligned}\frac{d}{dt}(\hat{e}_x) &= \frac{d}{dt}\hat{\mathbf{r}}_t \\ &= \frac{1}{r_t}[\dot{\mathbf{r}} - (\hat{\mathbf{r}} \cdot \dot{\mathbf{r}})\hat{\mathbf{r}}]\end{aligned}$$

For a two-body motion, the angular momentum and hence its direction does not change with time. That gives,

$$\frac{d}{dt}(\hat{e}_z) = 0 \tag{A.17}$$

Finally, the derivative of $\hat{e}_y$ has to be calculated,

$$\frac{d}{dt}(\hat{e}_y) = \frac{d}{dt}(\hat{e}_z \times \hat{e}_x) \tag{A.18}$$

$$= \left[\frac{d}{dt}(\hat{e}_z) \times \hat{e}_x\right] + \left[\hat{e}_z \times \frac{d}{dt}(\hat{e}_x)\right] \tag{A.19}$$

$$= \hat{e}_z \times \frac{d}{dt}(\hat{e}_x) \tag{A.20}$$

$$= \hat{\mathbf{h}}_t \times \frac{d}{dt}(\hat{e}_x) \tag{A.21}$$

Appendix B

DERIVATION OF HILL'S EQUATION AND SCHWEIGHART-SEDWICK EQUATIONS

We start by defining Hill's frame fixed on target spacecraft. The X-axis of the frame is radially outward from the center of primary body, in our case, it is Earth, Y-axis is in the direction of the velocity of the target and Z-axis is in the direction of angular momentum of the target and also completes the right-hand coordinate system. In inertial frame the location of target and chaser is $\mathbf{r}_t(t)$ and $\mathbf{r}_c(t)$ respectively. The position of chaser with respect to target is represented as $\mathbf{r}(t)$. Note that these positions are time-dependent and hence represented appropriately.

Acceleration due to gravity for both bodies are represented in inertial frame as,

$$\ddot{\mathbf{r}}_t(t) = \frac{-\mu}{r_t^3}\mathbf{r}_t(t) \tag{B.1}$$

$$\ddot{\mathbf{r}}_c(t) = \frac{-\mu}{r_c^3}\mathbf{r}_c(t) \tag{B.2}$$

Subsequently we get,

$$\begin{aligned}
\ddot{\mathbf{r}} &= \ddot{\mathbf{r}}_c - \ddot{\mathbf{r}}_t \\
&= -\mu\left(\frac{1}{r_c^3}\mathbf{r}_c(t) - \frac{1}{r_t^3}\mathbf{r}_t(t)\right) \\
&= -\mu\left(\frac{1}{r_c^3}(\mathbf{r}_t + \mathbf{r}) - \frac{1}{r_t^3}\mathbf{r}_t(t)\right)
\end{aligned}$$

Consider the term $\|\mathbf{r}_c\|^{-3}$ in the equation above, we will simplify it using the assumption that the relative distance between the two spacecraft is much lesser compared to the orbital radius of target(or chaser).

$$\begin{aligned}
\|\mathbf{r}_c\|^{-3} &= \|\mathbf{r}_t + \mathbf{r}\|^{-3} \\
&= \{(\mathbf{r}_t + \mathbf{r}) \cdot (\mathbf{r}_t + \mathbf{r})\}^{-3/2} \\
&= r_t^{-3}(1 - 3\frac{\mathbf{r}_t \cdot \mathbf{r}}{r_t^2} + \dots) \\
&\approx r_t^{-3}(1 - 3\frac{\mathbf{r}_t \cdot \mathbf{r}}{r_t^2}) \\
&= \frac{1}{r_t^3} - \frac{3}{r_t^5}(\mathbf{r}_t \cdot \mathbf{r})
\end{aligned}$$

Putting this back in previous expression for $\ddot{\mathbf{r}}$,

$$\begin{aligned}
\ddot{\mathbf{r}} &= \frac{-\mu}{r_t^3}\{[(1 - \frac{3(\mathbf{r}_t \cdot \mathbf{r})}{r_t^2})(\mathbf{r}_t + \mathbf{r})] - \mathbf{r}_t\} \\
&= \frac{-\mu}{r_t^3}\{\mathbf{r} - \frac{3(\mathbf{r}_t \cdot \mathbf{r})}{r_t^2}\mathbf{r}_t + \frac{3(\mathbf{r}_t \cdot \mathbf{r})}{r_t^2}\mathbf{r}\}
\end{aligned}$$

Again using the assumption that relative distance is much smaller than orbital radius, we can ignore the last term of the expression, which will give us final expression for $\ddot{\mathbf{r}}$

$$\ddot{\mathbf{r}} = \frac{-\mu}{r_t^3}\{\mathbf{r} - \frac{3(\mathbf{r}_t \cdot \mathbf{r})}{r_t^2}\mathbf{r}_t\} \tag{B.3}$$

Equation (B.3) expresses the relative acceleration in inertial frame. Now we want to express it in Hill's frame which is more relevant for this discussion and gives more useful expressions.

In frame attached at the center of Earth and axes aligned with Hill's frame, the position $\mathbf{r}_t$ is expressed as $r_t\hat{i}$, whereas $\mathbf{r}$ is expressed as $x\hat{i} + y\hat{j} + z\hat{k}$, Putting this in (B.3), we get

$$\ddot{\mathbf{r}} = -\frac{\mu}{r_t^3}(-2x\hat{i} + y\hat{j} + z\hat{k}) \tag{B.4}$$

The expression $\ddot{\mathbf{r}}$ expresses the dynamics in inertial frame. However we are interested in $\ddot{\mathbf{r}}_{rot}$ which expresses the dynamics of relative states in rotating Hill's frame attached on the target spacecraft.

$$\ddot{\mathbf{r}}_{rot} = \ddot{x}\hat{i} + \ddot{y}\hat{j} + \ddot{z}\hat{k} \tag{B.5}$$

From the expression relating acceleration in inertial and rotating frames, we know,

$$\ddot{\mathbf{r}}_{inertial} = \ddot{\mathbf{r}}_{rot} + 2\omega \times \dot{\mathbf{r}}_b + \dot{\omega} \times \mathbf{r} + \omega \times (\omega \times \mathbf{r}) \tag{B.6}$$

In this expression, $\mathbf{r} = x\hat{i} + y\hat{j} + z\hat{k}$ and $\dot{\mathbf{r}}_b = \dot{x}\hat{i} + \dot{y}\hat{j} + \dot{z}\hat{k}$. ω is the rotational rate of the frame with respect to inertial frame. Assuming that the target spacecraft is in a near circular orbit, the rotational rate of the Hill's frame is constant and is equal to mean motion n of the target spacecraft in $\hat{k}$ direction. This means $\omega = n\hat{k}$ and $\dot{\omega} = 0$ where $n^2 = \frac{\mu}{r_t^3}$. Putting all these in (B.6) along with (B.4) we get,

$$(2xn^2)\hat{i} + (-yn^2)\hat{j} + (-zn^2)\hat{k} = [\ddot{x}\hat{i} + \ddot{y}\hat{j} + \ddot{z}\hat{k}] + [-2n\dot{y}\hat{i} + 2n\dot{x}\hat{j}] + [-xn^2\hat{i} - yn^2\hat{j}]$$

$$(\ddot{x} - 2n\dot{y} - 3n^2x)\hat{i} + (\ddot{y} + 2n\dot{x})\hat{j} + (\ddot{z} + n^2z)\hat{k} = 0$$

Together these equations, combine to form what is known as Hill's equations.

$$\begin{aligned} \ddot{x} - 3n^2x - 2n\dot{y} &= 0 \\ \ddot{y} + 2n\dot{x} &= 0 \\ \ddot{z} + n^2z &= 0 \end{aligned} \tag{B.7}$$

A brief sketch of derivation of Schweighart-Sedwick equations is given here. For detailed derivation reader is suggested to read the original paper.

With J_2 effects the acceleration is written as,

$$\ddot{\mathbf{r}} = \mathbf{g}(\mathbf{r}) + \mathbf{J_2}(\mathbf{r}) \tag{B.8}$$

This expression is linearized about the trajectory of target spacecraft, which is in circular orbit,

$$\ddot{\mathbf{r}}_c = \mathbf{g}(\mathbf{r}_t) + \nabla\mathbf{g}(\mathbf{r}_t) \cdot \mathbf{r} + \mathbf{J}_2(\mathbf{r}_t) + \nabla\mathbf{J}_2(\mathbf{r}_t) \cdot \mathbf{r} \tag{B.9}$$

The terms in the equation above are expressed as

$$\mathbf{g}(\mathbf{r}_t) = -\left(\frac{\mu}{{r_t}^3}\right)\mathbf{r}_t \tag{B.10}$$

$$\nabla\mathbf{g}(\mathbf{r}_t) = \begin{bmatrix} 2\left(\frac{\mu}{{r_t}^3}\right) & 0 & 0 \\ 0 & -\left(\frac{\mu}{{r_t}^3}\right) & 0 \\ 0 & 0 & -\left(\frac{\mu}{{r_t}^3}\right) \end{bmatrix} \tag{B.11}$$

$$\mathbf{J}_2(\mathbf{r}_t) = -\left(\frac{3}{2}\right)\left(\frac{J_2\mu R_e^2}{{r_t}^4}\right)\left[(1 - 3\sin^2 i \sin^2\theta)\hat{i} + (2\sin^2 i \sin\theta\cos\theta)\hat{j} + (2\sin i \cos i \sin\theta)\hat{k}\right] \tag{B.12}$$

$$\nabla \mathbf{J}_2(\mathbf{r}_t, \theta, i) = \frac{6\mu J_2 R_e^2}{{r_t}^5} \begin{bmatrix} (1 - 3\sin^2 i \sin^2\theta) & \sin^2 i \sin 2\theta & \sin 2i \sin\theta \\ \sin^2 i \sin 2\theta & -\frac{1}{4} - \sin^2 i(\frac{1}{2} - \frac{7}{4}\sin^2\theta) & -\frac{\sin 2i \cos\theta}{4} \\ \sin 2i \sin\theta & -\frac{\sin 2i \cos\theta}{4} & -\frac{3}{4} + \sin^2 i(\frac{1}{2} + \frac{5}{4}\sin^2\theta) \end{bmatrix} \tag{B.13}$$

Since coordinate system is rotating,

$$\ddot{\mathbf{r}} = \ddot{\mathbf{r}}_\mathbf{c} - \ddot{\mathbf{r}}_\mathbf{t} - \mathbf{2}\omega \times \dot{\mathbf{r}} - \dot{\omega} \times \mathbf{r} - \omega \times (\omega \times \mathbf{r}) \tag{B.14}$$

Substituting equation (B.9) into the equation above we get,

$$\ddot{\mathbf{r}} + 2\boldsymbol{\omega} \times \dot{\mathbf{r}} + \dot{\boldsymbol{\omega}} \times \mathbf{r} + \boldsymbol{\omega} \times (\boldsymbol{\omega} \times \mathbf{r}) = \mathbf{g}(\mathbf{r}_t) + \nabla \mathbf{g}(\mathbf{r}_t) \cdot \mathbf{r} + \mathbf{J}_2(\mathbf{r}_t) + \nabla \mathbf{J}_2(\mathbf{r}_t) \cdot \mathbf{r} - \ddot{\mathbf{r}}_t \tag{B.15}$$

The significant contribution by Schweighart and Sedwick here is taking the time average of the gradient of J_2 term over an orbit, represented below,

$$\int_0^{2\pi} \nabla \mathbf{J}_2(\mathbf{r}_t)\, d\mu = \frac{\mu}{r_t^3} \begin{bmatrix} 4s & 0 & 0 \\ 0 & -s & 0 \\ 0 & 0 & -3s \end{bmatrix} \tag{B.16}$$

where

$$s \equiv (3J_2 R_e^2/8r^2)(1 + 3\cos 2i) \tag{B.17}$$

Building upon this foundation and through additional mathematical analysis, Schweighart and Sedwick developed the following equations, which account for the J_2 perturbation effects, thereby extending the classical Hill's equations to higher fidelity.

$$\begin{aligned} \ddot{x} - (5c^2 - 2)n^2 x - 2nc\dot{y} &= 0 \\ \ddot{y} + 2nc\dot{x} &= 0 \\ \ddot{z} + q^2 z &= 2lq\cos(qt + \phi) \end{aligned} \tag{B.18}$$

These equations use an updated angular velocity of rotating frame to account for J_2 effects, by introducing the term c, where,

$$c = \sqrt{1 + s}$$